University of Tennessee, Knoxville

TRACE: Tennessee Research and Creative Exchange

Masters Theses

Graduate School

12-2016

# Development, Analysis, and Optimization of a Swirl-Promoting Mean Flow Solution for Solid Rocket Motors

Andrew Steven Fist
*University of Tennessee, Knoxville*, afist@vols.utk.edu

Follow this and additional works at: https://trace.tennessee.edu/utk_gradthes

Part of the Aerodynamics and Fluid Mechanics Commons, Applied Mechanics Commons, Engineering Physics Commons, Propulsion and Power Commons, and the Space Vehicles Commons

## Recommended Citation

Fist, Andrew Steven, "Development, Analysis, and Optimization of a Swirl-Promoting Mean Flow Solution for Solid Rocket Motors. " Master's Thesis, University of Tennessee, 2016.
https://trace.tennessee.edu/utk_gradthes/4264

This Thesis is brought to you for free and open access by the Graduate School at TRACE: Tennessee Research and Creative Exchange. It has been accepted for inclusion in Masters Theses by an authorized administrator of TRACE: Tennessee Research and Creative Exchange. For more information, please contact trace@utk.edu.

To the Graduate Council:

I am submitting herewith a thesis written by Andrew Steven Fist entitled "Development, Analysis, and Optimization of a Swirl-Promoting Mean Flow Solution for Solid Rocket Motors." I have examined the final electronic copy of this thesis for form and content and recommend that it be accepted in partial fulfillment of the requirements for the degree of Master of Science, with a major in Mechanical Engineering.

Joseph C. Majdalani, Major Professor

We have read this thesis and recommend its acceptance:

Christian G. Parigger, Milton Davis Jr.

Accepted for the Council:
Carolyn R. Hodges

Vice Provost and Dean of the Graduate School

(Original signatures are on file with official student records.)

# Development, Analysis, and Optimization of a Swirl-Promoting Mean Flow Solution for Solid Rocket Motors

A Thesis Presented for the
Master of Science
Degree
The University of Tennessee, Knoxville

Andrew Steven Fist
December 2016

Copyright © 2016 by Andrew Fist
All rights reserved.

# Dedication

*This work is dedicated to my parents, Patricia and Steven, my brother Alex, and my partner Aleene. Their support and encouragement has allowed me to strive for success, and to make a difference in the lives of others. For their love I am forever thankful.*

# Acknowledgments

I would like to thank Dr. Majdalani who has inspired my interest in rocket propulsion, and who has provided incredible support throughout the development of this research. I would like to thank my additional committee members, Dr. Parigger and Dr. Davis, for their insight, advice and support through the thesis process. I would also like to thank Dr. Tony Saad for his foundational contributions to both my research and to the field.

# Abstract

This work demonstrates and analyses a new flow candidate for describing the internal gaseous motion in simulated rocket motors. The fundamental features of this solution include the conservation of key system properties also incorporated in the classic Taylor-Culick (TC) system (i.e. inviscid, axisymmetric, steady and rotational properties), while allowing for the development of a swirling velocity component. The work compares the new solution to the development and formulation of the classic TC system, ultimately identifying that both the new and classic solutions are special cases of the Bragg-Hawthorne equation. Following this development, the text then explores the development of energy-optimized variants utilizing Lagrangian optimization techniques. This effort demonstrates that multiple interesting energy states and associated velocity components may exist. The flow field properties are further evaluated, and both the base analytical solutions and its energy-optimized variants are verified via numeric integration techniques and the use of computational fluid dynamics.

# Table of Contents

**1** Introduction 1

1.1 Background ..... 1
1.2 Scope ..... 3
1.3 Format ..... 3
1.4 Methods ..... 4

**2** Framework Development 5

2.1 Geometric Configuration ..... 5
2.2 Boundary Conditions ..... 7
2.3 Normalization ..... 7

**3** Solution Formulation 9

3.1 Traditional Taylor-Culick Technique ..... 9
3.2 Bragg-Hawthorne Technique ..... 10
3.3 Beltramian Flow Solution via Bragg-Hawthorne Representation ..... 11
3.4 General and Partial Solutions ..... 12

**4** Results and Discussion 15

4.1 Flow Properties ..... 15

4.2 Comparison to the Taylor-Culick and Hart-McClure Mean Flows ..... 16
4.3 Numerical Verification of Exact Solution ..... 20
4.4 Flowfield Development Conclusions ..... 22

**5** Lagrangian Optimization of the Flowfield 23

5.1 Problem Definition ..... 23
5.2 Formulation of Solutions from the Bragg-Hawthorne Equation ..... 24
5.3 Solution Development Via Eigenfunction Expansion ..... 25
5.4 Kinetic Energy Optimization ..... 27
5.5 Large L Approximation for Slender Bodies ..... 30
5.6 Generalization of Energy Optimized Solution ..... 32

**6** Optimization Results and Discussion 37

6.1 Energy Density Analysis ..... 37
6.2 Pressure Analysis ..... 38
6.3 Numerical Verification of Energy-Steepened Solution ..... 40

**7** Conclusion 43

7.1 Significant Contributions ..... 43
7.2 Future Work ..... 44
7.3 Lessons Learned ..... 44
7.4 Personal Development ..... 46

References 47

Appendices 56

Appendix A – CFD Method Details ..... 57
Appendix B – Detailed CFD Results ..... 62

Vita 76

# List of Figures

Figure 2.1 Schematic of an idealized, cylindrical solid rocket motor. ..... 6

Figure 4.1 Comparison between streamlines of the new solution and those corresponding to the Taylor-Culick solution for a simulated SRM..... 17

Figure 4.2 Comparison between the Trkalian, Taylor-Culick, and Hart-McClure profiles. ..... 18

Figure 4.3 Depiction of uniform mesh structure utilized in CFD analysis ..... 20

Figure 4.4 Demonstration of agreement between CFD (circles) and analytical solutions (lines) of the proposed flowfield ..... 21

Figure 5.1 Depiction of the variation in energy density with increasing length, and demonstration of critical length concept. ..... 31

Figure 5.2 Variation of velocity distributions across the volume radius with increasing values of $q$. ..... 35

Figure 6.1 Depiction of energy density approaching an asymptote with increasing $q$ . ..... 38

Figure 6.2 Centerline Pressure Variation with increasing $q$. ..... 39

Figure 6.3 Verifying depiction of numerical (circles) and analytical solutions for transformed stream function equation $F(r) = \psi / z$ and its derivative. ..... 42

Figure B.1 Comparison of CFD (circles) and analytical results (lines) Case: Type I, Q=6; Pressure Scale Factor: 0.8933 ..... 63

Figure B.2 Comparison of CFD (circles) and analytical results (lines) Case: Type I, Q=5; Pressure Scale Factor: 0.9726 ..... 64

Figure B.3 Comparison of CFD (circles) and analytical results (lines) Case: Type I, Q=4; Pressure Scale Factor: 0.9455 ..... 65
Figure B.4 Comparison of CFD (circles) and analytical results (lines) Case: Type II, Q=6; Pressure Scale Factor: 1.0102 ..... 66
Figure B.5 Comparison of CFD (circles) and analytical results (lines) Case: Type II, Q=5; Pressure Scale Factor: .9996 ..... 67
Figure B.6 Comparison of CFD (circles) and analytical results (lines) Case: Type II, Q=4; Pressure Scale Factor: 1.066 ..... 68
Figure B.7 Comparison of Contours for Energy-Optimized Type I, Type II and Exact Solutions - Total Velocity Magnitude ..... 69
Figure B.8 Comparison of Contours for Energy-Optimized Type I, Type II and Exact Solutions - Axial Velocity ..... 70
Figure B.9 Comparison of Contours for Energy-Optimized Type I, Type II and Exact Solutions - Axial Velocity ..... 71
Figure B.10 Comparison of Contours for Energy-Optimized Type I, Type II and Exact Solutions - Swirl Velocity ..... 72
Figure B.11 Comparison of Contours for Energy-Optimized Type I, Type II and Exact Solutions – Stream Function..... 73
Figure B.12 Comparison of Contours for Energy-Optimized Type I, Type II and Exact Solutions – Static Pressure..... 74
Figure B.13 Comparison of Contours for Energy-Optimized Type I, Type II and Exact Solutions – Total Pressure ..... 75

# List of Symbols

$A_i$ = inlet area

$a$ = chamber radius

$B$ = tangential angular momentum, $ru_\theta$

$H$ = stagnation pressure head

$L$ = chamber length

$l$ = chamber aspect ratio, $L / a$

$p$ = pressure

$Q_i$ = inlet volumetric flow rate

$r, \theta, z$ = radial, tangential, and axial coordinates

$U_c$ = headwall injection velocity

$U_w$ = sidewall inflow velocity

$u_r$ = dimensional radial velocity

$u_\theta$ = dimensional tangential velocity

$u_z$ = dimensional axial velocity

$\mathbf{V}$ = velocity vector

$\kappa$ = off-swirl Ekman number

$\lambda_n$ = nth zero of $J_1$, the Bessel function of the first kind

$\sigma$ = swirl number, $a^2 / A_i$

$\upsilon$ = separation constant

$\psi$ = stream function

$\bar{}$ = overbars denote a non-dimensional variable

$\omega$ = vorticity

# Chapter 1

# Introduction

## 1.1 Background

In the field of rocketry, the use of analytical bulk flow models, derived from first principles, has proved invaluable to the preliminary design of rocket motors, and the exploration of more complicated phenomena. Most notably, the inviscid flow model presented by Culick[1] has become a nexus for the study of numerous propulsion and aero-acoustic challenges, and as a result has supported numerous analytical, simulation, and experimental studies. Originally developed to support the study of solid rocket motors (SRMs), the Taylor-Culick (TC) model, as it is known, may be considered a steady, rotational, axisymmetric, inviscid, and incompressible representation of the Euler momentum equations. Driven by pressure forces in a frictionless environment, the model is particularly useful in that it was carefully developed to satisfy the "no-slip" condition that exists at the solid fuel sidewall of an SRM, in which gaseous particles join the gas flowfield as the fuel pyrolizes.

As a result of these characteristics, the model has attracted its use in a number of study topics to include:

- Acoustic instability and prediction methods[2-6], which have demonstrated that the Taylor-Culick model is capable of providing an adequate mean flow velocity to which small amplitude oscillations may be superimposed.

- Effects of metallized particle loading in the flow and associated particle-mean flow interactions and its implications for hydrodynamic stability[7-14]
- Bulk kinematic speeds and particle accelerations important to the study of hybrid rocket motors[15-17]
- Reactive Flow simulations and the validation of associated CFD codes, to include Chu, Yang and Majdalani's premixed propane-air simulations of internally burning solid propellants,[18] Venugopal, Moser and Najjar's compressible Navier-Stokes computations of the injection-driven motion in SRMs with homogenous grains,[19] and Chedevergne, Casalis and Majdalani's direct numerical simulations of both mean and unsteady flow structures evolving in SRMs.[6]

While valuable in its original form and construction, substantial work has been presented over decades of research to improve the underlying model to accommodate additional flow phenomena, to include:

- Modification of the base flow to capture the effects of viscous shear layers and receding grain surfaces[20-23]
- Development of a semi-analytical approach to account for the effects of non-circular cross-sections[24]
- Prediction of high-speed flow conditions utilizing a Rayleigh-Jensen expansion and associated fluid dilatation[25, 26]
- Accommodation of arbitrary headwall injection[27]
- Development of a reduced compressible Euler form for slender bodies and uniform and non-uniform wall fluxes[28-31]
- Exploration of additional kinetic energy states based on Lagrangian optimization principles.[32, 33]

Regarding the verification of the flow field, a collective body of research has examined the TC shape and spatial development in a series of dedicated investigations, beginning with laboratory experiments by Taylor himself[34]. From there, a number of computational [35-38], experimental[39-42], and theoretical[43-47] studies for cylindrical and planar motors configurations. Most of these studies confirm the suitability of the TC model in the role of approximating the

bulk flow in a simulated SRM[48], however, many seem to recognize the natural tendency of the flow to develop a nonzero swirl component, with attendant axial vorticity, in long chambers with circular cross section.[16, 40]. These studies would specifically include the classic cold flow simulations of solid rocket motors by Dunlap et al.,[40] which served for years as a valuable source for measured mean and oscillatory flowfields in cylindrical configurations with transpiring walls. The data obtained in those experiments exhibited a tangential, swirling component of motion, which has frequently been overlooked or ignored in subsequent formulations of the problem.

Naturally, such a swirl component, when present, would comprise a portion of the flow's total kinetic energy, affect downstream interaction and thrust production with a nozzle system, and may affect other acoustic and bulk flow interactions so significantly studied by the community. Additionally, it is plausible that such swirling flows would be present if not exacerbated by viscous effects in spin-stabilized rocket motor applications, and the presence of an analytical, closed-form tool would be a boon to its study. For this reason, effort was undertaken to understand if the methods comprising the TC construction could accommodate other formulations that allowed for a swirling field to develop.

## 1.2 Scope

The purpose of this text is to communicate the body of research concerning the development and validation of a new inviscid flowfield, which is believed to be suitable for describing the flow in a solid rocket motor. This new field possesses the unique feature of allowing the development of a swirling velocity component. Furthermore, the field is evaluated using optimization techniques that demonstrate that a family of solutions can be produced that possess varying kinetic energy contents.

## 1.3 Format

This work is logically arranged to accessibly convey the nuance of the study at hand, and its relevance and contribution to the body of knowledge for the field. Chapter 1 provides a historical primer in relevant flow field studies and their utility to academic discourse, and outlines the work to be discussed throughout the text. Chapter 2 will develop the analytical framework, to include problem description, boundary conditions, and normalization methods that

are appropriate both for the historical effort and the new contribution. Chapter 3 serves to accomplish two goals – to both explain the methods of achieving the historical flow fields, and then offer an alternative construction that results in the new flow field under study in this work. Chapter 4 will then analyze and assess the properties of the newly defined field. In Chapter 5, energy-based optimization methods are explored that reveal other solutions in the family that satisfy the underlying first-principles equations and boundary equations, with the content of kinetic energy in each field being a discriminator. Chapter 6 will probe the results of the optimization study, and provide additional confirmation of the methods using numeric approximation and finite-element techniques. Finally, Chapter 7 will draw conclusions from the full body of effort, and will describe opportunities for future research.

It is hoped that through this work the body of research and its relevance are readily communicated, with the validation methods presented providing an additional degree of confidence in the results.

## 1.4 Methods

Throughout this research, a number of tools were used to aid in the task of developing and communicating the results. Mathematical computation software (Mathematica 10.4™) was utilized to aid in the computation of particular elements of the underlying flowfield solution, particularly when terms utilized summation notations. The tool was also used to perform the numerical approximation techniques described in the text. For the finite-element techniques described, ANSYS Workbench 17.0™ and FLUENT 17.0™ tools were utilized to instantiate and provide solutions. These solutions were developed using a desktop personal computer with an Intel Core™ i7-4770K processor, operating eight parallel threads. Finally, the visual communication tool OriginPro 2016™ was utilized to develop and convey chart content when typical word-processing tools would not suffice. Select methods used in the development of this document are appended to this text, in order to allow the reader to develop a further appreciation for the analysis techniques.

# Chapter 2

# Framework Development

This chapter will develop and present the typical framework utilized to evaluate flow field solutions. This framework builds upon the effort first presented in utilized throughout the research[49-51] and is sufficiently common to allow for the comparison of the new solution relative to classic flow fields. Specifically, the chapter establishes a normalized description of the geometry & boundary conditions of an idealized solid rocket motor, and describes a format for the physical governing equations that will be used throughout the work. As this research has been well communicated to the community over the course of its development, the methods presented in the subsections of this chapter have been previously published by the author and his advisor[49-51], and are foundational to the remainder of the text.

## 2.1 Geometric Configuration

The geometry of an idealized SRM is classically considered to be a right cylindrical enclosure. As shown in Figure 2.1, it consists of a porous sidewall of length $L$ and radius $a$, a nozzleless aft closure, and the potential for either a reactive or non-reactive headwall. Flow velocities are represented as $(\bar{u}_r, \bar{u}_\theta, \bar{u}_z)$, indicating radial, tangential, and axial velocities accordingly. The corresponding spatial coordinates are given by $(\bar{r}, \theta, \bar{z})$, where $0 \le \bar{r} \le a$, $0 \le \theta \le 2\pi$ and $0 \le \bar{z} \le L_0$ define the range over which the solution may be extended,

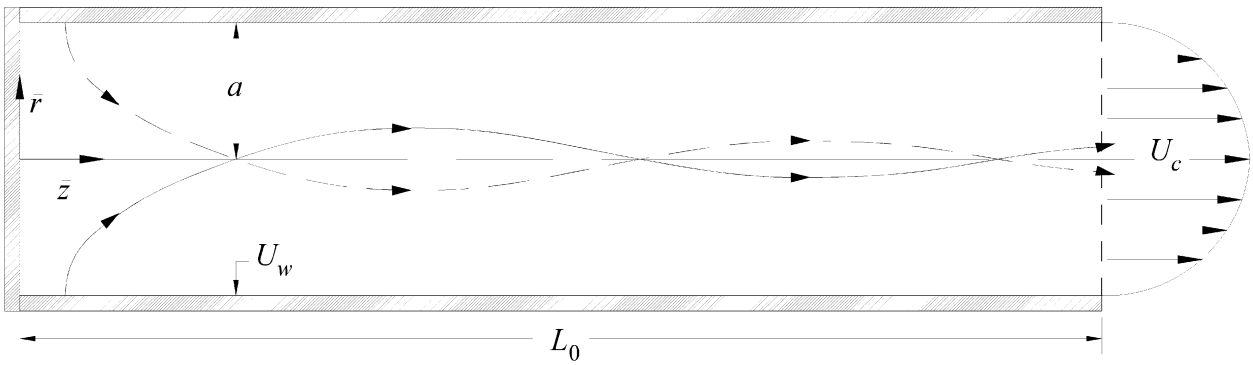


**Figure 2.1 Schematic of an idealized, cylindrical solid rocket motor.**

specifically from the headwall to the typical nozzle attachment point in the chamber exit plane. In the case of an axisymmetric configuration, such as the model under consideration, dependence on $\theta$ can be relaxed. Variables with overbars denote dimensional quantities. In more advanced models, fluid injection at the head wall may be permitted, to simulate a reactive headwall, or injection of additional oxidizer. Velocities for such headwall injection may be user defined, as identified by Majdalani and Fist[49], however the focus of this text will remain on a non-reacting, inert headwall. This profile may be described as $\bar{u}_0(\bar{r})$ in the following manner

$$\bar{u}_0(\bar{r}) = \bar{u}_z(\bar{r},0) = \begin{cases} 0 & \text{inert headwall} \\ U_c \cos(\tfrac{1}{2}\pi\bar{r}^2/a^2) & \text{Berman (half-cosine) – complex lamellar flow} \\ U_c J_0(j_{0,1}\bar{r}/a) & \text{Bessel – Beltramian flow} \end{cases} \tag{2.1}$$

where $j_{0,1}$ denotes the first root of the zeroth-order Bessel function of the first kind. The headwall injection velocity, $U_c = \bar{u}_z(0,0)$, indicates the centerline speed a the headwall location, which in the case of an inert headwall, may be set to zero. In the cases where the headwall is not inert, the axial stream will merger with the sidewall flows entering perpendicularly. In the case of simulated solid rocket motors in which both the headwall and sidewall represent slowly pyrolizing fuels, the magnitudes of headwall velocity $U_c$ and sidewall velocity $U_w$ will be comparable.

## 2.2 Boundary Conditions

The boundary conditions utilized are identical to those used in the development of the classic Taylor-Culick solution. The conditions are developed from an axisymmetric configuration and wall-normal sidewall injection. In a manner consistent with the original TC model, swirl is prohibited at the headwall. These conditions are described as

(a) a vanishing radial velocity along the axis of symmetry: $\bar{u}_r(0,\bar{z}) = 0$

(b) a vanishing axial velocity at the sidewall, (a no-slip condition): $\bar{u}_z(a,\bar{z}) = 0$

(c) a uniform injection at the sidewall: $\bar{u}_r(a,\bar{z}) = -U_w$

(d) a prescribed injection pattern at the headwall: $\bar{u}_z(\bar{r},0) = \bar{u}_0(\bar{r})$

(e) a vanishing swirl velocity at the headwall: $\bar{u}_\theta(a,0) = 0$

This last condition is critical to the proper derivation of the TC profile, where it is implicitly applied. Otherwise, a free vortex motion may evolve as shown by Balachandar, Buckmaster and Short[16] in their work studying axial vorticity distribution in simulated solid-propellant rocket motor flows.

## 2.3 Normalization

The relevant flow field parameters may be appropriately normalized by utilizing as reference values the radius $a$ and the sidewall injection speed $U_w$ to provide:

$$\begin{gathered} r = \frac{\bar{r}}{a};\ z = \frac{\bar{z}}{a};\ u_r = \frac{\bar{u}_r}{U_w};\ u_\theta = \frac{\bar{u}_\theta}{U_w};\ u_z = \frac{\bar{u}_z}{U_w};\ p = \frac{\bar{p}}{\bar{\rho}U_w^2}; \\ \boldsymbol{\Omega} = \frac{\bar{\boldsymbol{\Omega}}a}{U_w};\ \psi = \frac{\bar{\psi}}{a^2U_w};\ \nabla = a\bar{\nabla};\ L = \frac{L_0}{a};\ u_0 = \frac{\bar{u}_0}{U_w};\ u_c = \frac{U_c}{U_w} \end{gathered} \tag{2.2}$$

where $(\bar{p},\bar{\rho},\bar{\boldsymbol{\Omega}},\bar{\psi})$ indicate pressure, density, vorticity and stream function, respectively. Because the flow is identified to be inviscid, rotational, incompressible, axisymmetric, and steady, Euler's normalized momentum equation may be reduced to $\nabla p = \boldsymbol{u}\times\boldsymbol{\Omega} - \frac{1}{2}\nabla(\boldsymbol{u}\cdot\boldsymbol{u})$. The pressure may be eliminated by curling Euler's equation, which results into the steady-state vorticity transport equation (VTE), $\nabla\times(\boldsymbol{u}\times\boldsymbol{\Omega}) = 0$. Additionally, continuity $\nabla\cdot\boldsymbol{u} = 0$ may be imposed through the utilization of the Stokes stream function,

$$u_r = -\frac{1}{r}\frac{\partial \psi}{\partial z} \quad \text{and} \quad u_z = \frac{1}{r}\frac{\partial \psi}{\partial r} \tag{2.3}$$

With this relation in hand, the auxiliary conditions can be re-written as

$$\begin{cases} u_r(0,z) = \lim\limits_{r\to 0}\dfrac{1}{r}\dfrac{\partial \psi(r,z)}{\partial z} = 0 & \text{(a)} \\ u_z(1,z) = \dfrac{\partial \psi(1,z)}{\partial r} = 0 & \text{(b)} \\ u_r(1,z) = -\dfrac{\partial \psi(1,z)}{\partial z} = -1 & \text{(c)} \\ u_z(r,0) = \dfrac{1}{r}\dfrac{\partial \psi(r,0)}{\partial r} = u_0 & \text{(d)} \\ u_\theta(1,0) = 0 & \text{(e)} \end{cases} \qquad u_0(r) = \begin{cases} 0 & \text{inert headwall} \\ u_c \cos(\tfrac{1}{2}\pi r^2);\ u_c = \pi u_h \approx 3.14159 u_h & \text{Berman} \\ u_c J_0(j_{0,1} r);\ u_c = \dfrac{u_h j_{0,1}}{J_1(j_{0,1})} \approx 4.63226 u_h & \text{Bessel} \end{cases} \tag{2.4}$$

Lastly, the limiting condition at $r = 0$ may be rewritten via L'Hôpital's Rule to produce two equivalent forms useful for the impending analysis, namely

$$\frac{\partial \psi(0,z)}{\partial z} = 0 \quad \text{(a)} \qquad \text{and} \qquad \frac{\partial^2 \psi(0,z)}{\partial r \partial z} = 0 \quad \text{(b).} \tag{2.5}$$

In normalized form, the continuity and inviscid equations of motion may now be written as

$$\frac{1}{r}\frac{\partial (r u_r)}{\partial r} + \frac{\partial u_z}{\partial z} = 0 \tag{2.6}$$

$$u_r \frac{\partial u_r}{\partial r} + u_z \frac{\partial u_r}{\partial z} - \frac{u_\theta^2}{r} = -\frac{\partial p}{\partial r} \tag{2.7}$$

$$u_r \frac{\partial u_z}{\partial r} + u_z \frac{\partial u_z}{\partial z} = -\frac{\partial p}{\partial z} \tag{2.8}$$

# Chapter 3

# Solution Formulation

This chapter will build up from a demonstration of the traditional flow field solution developed by Taylor and Culick, and then:

- Present the Bragg Hawthorne Equation as a reduced form of the Euler momentum equations
- Show how the BHE can produced the TC solution when certain relations are made
- Show how the new solution can be produced alternative but also valid relations

As this research has been well communicated to the community over the course of its development, the methods presented in the subsections of this chapter have been previously published by the author and his advisor [49-51], and are foundational to the remainder of the text.

## 3.1 Traditional Taylor-Culick Technique

In the classic solution by Culick[1], the effort progresses by eliminating the pressure and velocities by instead describing the field in terms of vorticity and the Stokes streamfunction. By identifying a relation between vorticity and streamfunction that satisfies the VTE, a second order PDE is created by substituting the relation into the vorticity equation, $\boldsymbol{\Omega} = \nabla \times \boldsymbol{u}$. Subsequently, this PDE may be solved for the streamfunction $\psi$. Culick[1] shows that the use of $\Omega_\theta = r\ \Xi(\psi)$ and its compliment, $\Xi = \mathcal{C}^2\psi$ both satisfies the VTE and produces the PDE

$$\frac{\partial^2\psi}{\partial z^2}+\frac{\partial^2\psi}{\partial r^2}-\frac{1}{r}\frac{\partial\psi}{\partial r}+\mathcal{C}^2r^2\psi=0 \tag{3.1}$$

The use of separation of variables and a zero separation constant produce

$$\psi=(c_1z+c_2)[c_3\sin(\tfrac{1}{2}\mathcal{C}r^2)+c_4\cos(\tfrac{1}{2}\mathcal{C}r^2)]. \tag{3.2}$$

The remaining constants of Eq. (3.2) may be revealed via application of the auxiliary Eq. (2.4), with the use of Eq. (2.5) to facilitate the replacement of the limit in (2.4)a. As a result, the second element of Eq. (2.5) becomes self-satisfying. Following this, and if a similarity-conforming injection pattern at the headwall is assumed, i.e. $u_0(r)=u_c\cos(\tfrac{1}{2}\pi r^2)$, then the extended TC profile may be identified as

$$\begin{aligned}&\psi=(z+u_h)\sin(\tfrac{1}{2}\pi r^2);u_h\equiv u_c/\pi;\\&\boldsymbol{\Omega}=\pi^2(z+u_h)r\sin(\tfrac{1}{2}\pi r^2)\boldsymbol{e}_\theta;\\&\boldsymbol{u}=-\frac{1}{r}\sin(\tfrac{1}{2}\pi r^2)\boldsymbol{e}_r+\pi(z+u_h)\cos(\tfrac{1}{2}\pi r^2)\boldsymbol{e}_z\end{aligned} \tag{3.3}$$

It is important to note that Eq. (2.4)e, which would inhibit the presence of swirl, is implicitly utilized, which leads to a vanishing tangential velocity component. In the text that follows, it will be demonstrated that the above construction is directly recoverable from the Bragg-Hawthorne equation, where the implications of the no swirl requirement will be discussed.

## 3.2 Bragg-Hawthorne Technique

The Bragg-Hawthorne equation (BHE) is a reduced, scalar equivalent of Euler's equation, which may be developed in solutions possessing steady flow and axisymmetry. Also known as the Squire-Long equation, it is identified by Batchelor[52] as a PDE relating the stream function $\bar{\psi}$ to the angular momentum $\bar{B}=\bar{r}\bar{u}_\theta$ and total fluid head $\bar{H}=\bar{p}/\bar{\rho}+\tfrac{1}{2}\bar{\boldsymbol{u}}\cdot\bar{\boldsymbol{u}}$. In dimensional form, it may be written as

$$\frac{\partial^2\bar{\psi}}{\partial\bar{r}^2}-\frac{1}{\bar{r}}\frac{\partial\bar{\psi}}{\partial\bar{r}}+\frac{\partial^2\bar{\psi}}{\partial\bar{z}^2}=\bar{r}^2\frac{\mathrm{d}\bar{H}}{\mathrm{d}\bar{\psi}}-\bar{B}\frac{\mathrm{d}\bar{B}}{\mathrm{d}\bar{\psi}} \tag{3.4}$$

and a non-dimensional form may be developed using $B=\bar{B}/(aU_w)$ and $H=\bar{H}/U_w^2$ to produce

$$\frac{\partial^2\psi}{\partial r^2}-\frac{1}{r}\frac{\partial\psi}{\partial r}+\frac{\partial^2\psi}{\partial z^2}=r^2\frac{\mathrm{d}H}{\mathrm{d}\psi}-B\frac{\mathrm{d}B}{\mathrm{d}\psi} \tag{3.5}$$

where $B = ru_\theta$ and $H = p + \frac{1}{2}\boldsymbol{u}\cdot\boldsymbol{u}$. It is evident by the form of Eq. (3.5) that the vorticity-stream function method is well-suited to produce solutions that may be readily compared to the TC solution. By way of example, Eq.(3.1) used by Culick[1] may be directly recovered from Eq. (3.5) by assuming a constant angular momentum and a total head that varies with $\psi^2$. Such assumptions may be written as

$$B\frac{\mathrm{d}B}{\mathrm{d}\psi}=0 \qquad B(\psi)=B_0=\text{const.} \quad \text{or} \quad u_\theta=\frac{B_0}{r} \tag{3.6}$$

where $B_0 = 0$ is applied to eliminate the development of axial swirl. The second assumption translates into a constant stagnation head along a streamline, which may be written as

$$\frac{\mathrm{d}H}{\mathrm{d}\psi}=-\mathcal{C}^2\psi \quad \text{or} \quad H(\psi)=-\tfrac{1}{2}\mathcal{C}^2\psi^2+H_0 \tag{3.7}$$

where $H_0$ is a constant. These assumptions permit the reduction of the BHE into Eq. (3.1), such that the classic TC solution may be produced. Similarly, Vyas and Majdalani[53] utilize this same framework to explore cyclonic flows and bidirectional vortex motion in a similarly bounded problem by utilizing the BHE and similar assumptions other than a non-vanishing $B_0 = 1$. The resulting flowfield is described as

$$\begin{aligned}&\psi=\kappa z\sin(\pi r^2); \quad \boldsymbol{\Omega}=4\pi^2 rz\sin(\pi r^2)\boldsymbol{e}_\theta;\\ &\boldsymbol{u}=-\kappa r^{-1}\sin(\pi r^2)\boldsymbol{e}_r+r^{-1}\boldsymbol{e}_\theta+2\pi\kappa z\cos(\pi r^2)\boldsymbol{e}_z\end{aligned} \tag{3.8}$$

In which solution exists an off-swirl Ekman number, $\kappa = a/(2\pi\sigma L_0)$, and $\sigma$ describes the swirl number.

## 3.3 Beltramian Flow Solution via Bragg-Hawthorne Representation

In the process of identifying alternative flowfields that satisfy the problem constraints, we may begin by evaluating the flexibility the BHE provides regarding the relation between total head and angular momentum. For example, Majdalani[54] shows in his study of cyclonic motion that a viable set of assumptions may include a globally constant stagnation head, i.e.,

$$\frac{\mathrm{d}H}{\mathrm{d}\psi} = 0 \text{ or } H(\psi) = H_0 = \text{const.} \tag{3.9}$$

which, critically, may be implemented in conjunction with an angular momentum rate that obeys,

$$B\frac{\mathrm{d}B}{\mathrm{d}\psi} = \mathcal{C}^2\psi \qquad B^2 = \mathcal{C}^2\psi^2 + \mathcal{D}, \quad \text{or} \quad u_\theta = \frac{\sqrt{\mathcal{C}^2\psi^2 + \mathcal{D}}}{r} \tag{3.10}$$

and the non-dimensional forms of $\mathcal{C}$ and $\mathcal{D}$ correspond to

$$\mathcal{C} = \bar{\mathcal{C}}a \quad \text{and} \quad \mathcal{D} = \frac{\bar{\mathcal{D}}}{U_w^2 a^2}. \tag{3.11}$$

Finally, consistent with Eqs. (3.9) and (3.10), Eq. (3.5) resolves to

$$\frac{\partial^2\psi}{\partial r^2} - \frac{1}{r}\frac{\partial\psi}{\partial r} + \frac{\partial^2\psi}{\partial z^2} + \mathcal{C}^2\psi = 0 \tag{3.12}$$

## 3.4 General and Partial Solutions

Informed by the linear nature of Eq. (3.12), a separable solution form $\psi(r,z) = f(r)g(z)$ may be utilized. Inputting this into the solution results in

$$-\frac{\ddot{g}(z)}{g(z)} = \frac{1}{f}\left(f'' - \frac{1}{r}f' + \mathcal{C}^2 f\right) = \begin{cases} 0 & \text{(type 0)} \\ +\upsilon^2 & \text{(type I)} \\ -\upsilon^2 & \text{(type II)} \end{cases} \tag{3.13}$$

and, considering each of the separation constants, streamfunction solutions resolve as

$$\psi(r,z) = \begin{cases} r(c_1 z + c_2)\left[c_3 J_1(\mathcal{C}r) + c_4 Y_1(\mathcal{C}r)\right]; & \text{(type 0)} \\ r\left[c_1\sin(\upsilon z) + c_2\cos(\upsilon z)\right]\left[c_3 J_1(r\sqrt{\mathcal{C}^2 - \upsilon^2}) + c_4 Y_1(r\sqrt{\mathcal{C}^2 - \upsilon^2})\right]; & \text{(type I)} \\ r\left[c_1\sinh(\upsilon z) + c_2\cosh(\upsilon z)\right]\left[c_3 J_1(r\sqrt{\mathcal{C}^2 + \upsilon^2}) + c_4 Y_1(r\sqrt{\mathcal{C}^2 + \upsilon^2}\right]; & \text{(type II)} \end{cases} \tag{3.14}$$

In order to address practical flowfields that may describe SRMs, we focus initially on partial solutions of type 0, as they may most readily be compared to the work of Culick,[1] Majdalani,[54] and Vyas and Majdalani.[53]

In any case, to address the singularity that manifests at $r \to 0$ we must set $c_4 = 0$, which also satisfies Eq. (2.4)a, provided that the centerline is indeed part of the fluid domain which in

the case under study it would (an alternative configuration might include the incorporation of a centerbody structure to the field, which is not in the scope of this study). Without losing generality, we may set $c_3 = 1$ and write for the type 0 solution

$$\psi(r,z) = r(c_1 z + c_2) J_1(\mathcal{C} r) \tag{3.15}$$

Next, the application of the no-slip condition may be performed to result in

$$u_z(1,z) = \mathcal{C}(c_1 z + c_2) J_0(\mathcal{C}) = 0; \forall z \quad \text{or} \quad J_0(\mathcal{C}) = 0 \tag{3.16}$$

At this juncture, the eigencondition for the problem is identified, with the eigenvalues being zeroes of the zeroth-order Bessel function of the first kind, $\mathcal{C} = j_{0,m} = \{2.40483, 5.52008, 8.65373, \ldots\}; m = 1,2,3,\ldots$ Furthermore the partial solution currently under analysis may be linked to only first zero, specifically, $\mathcal{C} = j_{0,1} = 2.40483,$ which is similar in function to the TC constant of $\pi = 3.14159.$ Higher zeroes are not evaluated as they lead to recirculatory regions that do not correspond to the SRM problem at hand. At this point, the first eigenvalue will be referred to as $\lambda_1 = j_{0,1}$ to simplify notation.

Now that $\mathcal{C}$ has been determined, the second constraint related to the sidewall may be applied on the radial velocity to produce

$$u_r(1,z) = -c_1 J_1(\lambda_1) = -1; \forall z \quad \text{or} \quad c_1 = 1 / J_1(\lambda_1) \tag{3.17}$$

which now further simplifies the streamfunction description to

$$\psi = r[z + c_2 J_1(\lambda_1)] J_1(\lambda_1 r) / J_1(\lambda_1)\,. \tag{3.18}$$

In the case of the inert headwall, the fourth condition may be applied to recover $c_2 = 0$, or more generally, if a similarity-conforming Bessel function at the headwall is assumed, we may retrieve

$$u_z(r,0) = c_2 \lambda_1 J_0(\lambda_1 r) = u_c J_0(j_{0,1} r); \forall r \quad \text{or} \quad c_2 = u_c / \lambda_1 \tag{3.19}$$

Again, the streamfunction description can now be further re-written as

$$\psi(r,z) = r\left[z + \frac{u_c J_1(\lambda_1)}{\lambda_1}\right] \frac{J_1(\lambda_1 r)}{J_1(\lambda_1)} = r(z + u_h) \frac{J_1(\lambda_1 r)}{J_1(\lambda_1)}; \quad u_h \equiv u_c \frac{J_1(\lambda_1)}{\lambda_1} \tag{3.20}$$

where this form now describes a headwall constant that is consistent with a similarity-conforming axial injection speed applied at the headwall. The final condition, provided by Eq.

(2.4)e, prohibits the development of swirl at the headwall. In coordination with Eq. (3.10), we produce

$$u_\theta(1,0) = \sqrt{\lambda_1^2 u_h^2 + \mathcal{D}} = 0 \quad \text{or} \quad \mathcal{D} = -\lambda_1^2 u_h^2 \tag{3.21}$$

Finally, for tangential velocity, we produce

$$\begin{gathered} u_\theta = \frac{\lambda_1}{r}\sqrt{r^2(z+u_h)^2 \frac{J_1^2(\lambda_1 r)}{J_1^2(\lambda_1)} - u_h^2} = \frac{\lambda_1(z+u_h)}{z_h}\frac{J_1(\lambda_1 r)}{J_1(\lambda_1)}; \\ z_h \equiv \frac{(z+u_h) r J_1(\lambda_1 r)}{\sqrt{(z+u_h)^2 r^2 J_1^2(\lambda_1 r) - u_h^2 J_1^2(\lambda_1)}} \end{gathered} \tag{3.22}$$

where $z_h = 1$ when $u_h = 0$. From here, the properties of the flowfield will be further explored.

# Chapter 4

# Results and Discussion

Now that a new streamfunction solution has been developed via the Bragg-Hawthorne equation, relations may be developed that link particle velocity, associated vorticity and pressure to the newly obtained stream function, as well as the streamlines that it describes. As this research has been well communicated to the community over the course of its development, the methods presented in the subsections of this chapter have been previously published by the author and his advisor[49-51], and again are foundational to the remainder of the text. One exception is the content regarding numerical verification of the new solution presented, which has been submitted for publication[55].

## 4.1 Flow Properties

We recall from the beginning of the solution process that the Stokes streamfunction was used as a replacement for velocity components - and by extension, vorticity and pressure scalars - and as a result, those values may now be recovered from Eq. (3.20). To start, we retrieve the radial and axial velocities,

$$\begin{aligned} u_r &= -J_1(\lambda_1 r)/J_1(\lambda_1) \approx -1.92623 J_1(\lambda_1 r); \\ u_z &= \lambda_1 (z+u_h) J_0(\lambda_1 r)/J_1(\lambda_1) \approx 4.63226 (z+u_h) J_0(\lambda_1 r) \end{aligned} \tag{4.1}$$

In evaluating Eq. (4.1) , it is identified that the equation shares similar properties to the classic TC model, in that both maintain a radial speed that is independent of axial position, while the axial speed increases linearly as the distance from the headwall increases. Written in vector form, the velocity profile can be summarized as

$$\boldsymbol{u} = -J_1^{-1}(\lambda_1)J_1(\lambda_1 r)\boldsymbol{e}_r + \lambda_1(z+u_h)z_h^{-1}J_1^{-1}(\lambda_1)J_1(\lambda_1 r)\boldsymbol{e}_\theta + \lambda_1(z+u_h)J_1^{-1}(\lambda_1)J_0(\lambda_1 r)\boldsymbol{e}_z \tag{4.2}$$

Similarly, the vorticity may be summarized as

$$\begin{aligned}\boldsymbol{\Omega} = &-z_h\lambda_1 J_1^{-1}(\lambda_1)J_1(\lambda_1 r)\boldsymbol{e}_r \\ &+(z+u_h)\lambda_1^2 J_1^{-1}(\lambda_1)J_1(\lambda_1 r)\boldsymbol{e}_\theta \\ &+z_h(z+u_h)\lambda_1^2 J_1^{-1}(\lambda_1)J_0(\lambda_1 r)\boldsymbol{e}_z\end{aligned} \tag{4.3}$$

where in both cases the headwall corrective multiplier of $z_h = 1$ may be used in the case that an inert headwall is present. The above forms for velocity and vorticity also allow the ability to demonstrate the Beltramian nature of the flow, that is, that the velocity and vorticity fields are always locally parallel. Inspection of those forms reveals that character because $\boldsymbol{\Omega} / \boldsymbol{u} = z_h\lambda_1$, thus demonstration local parallelism, which in turn can further reduce to a global constant, $\lambda_1$, in the cases that $u_h = 0.$. An inert headwall will satisfy such a condition, in which case the flow solution, with a globally invariant constant relating velocity and vorticity are known as *Trkalian*.[54] Finally, the pressure distribution may be recovered from Euler's momentum equation, in which the partial integration and recombination provide

$$p = \tfrac{1}{2}r^{-2}\left(u_h^2\lambda_1^2 + \left\{u_h^2\lambda_1^2 - J_1^2(\lambda_1 r) - (u_h+z)^2\lambda_1^2\left[J_0^2(\lambda_1 r) + J_1^2(\lambda_1 r)\right]\right\}J_1^{-2}(\lambda_1)r^2\right) \tag{4.4}$$

Following this identification of the flow properties, each will be evaluated against the corresponding Taylor-Culick and Hart-McClure flow parameters, namely the axial & radial velocities and the streamline turning angle.

## 4.2 Comparison to the Taylor-Culick and Hart-McClure Mean Flows

The comparison between the Trkalian, Beltramian, and TC solutions may begin with a comparison of their streamlines, shown in

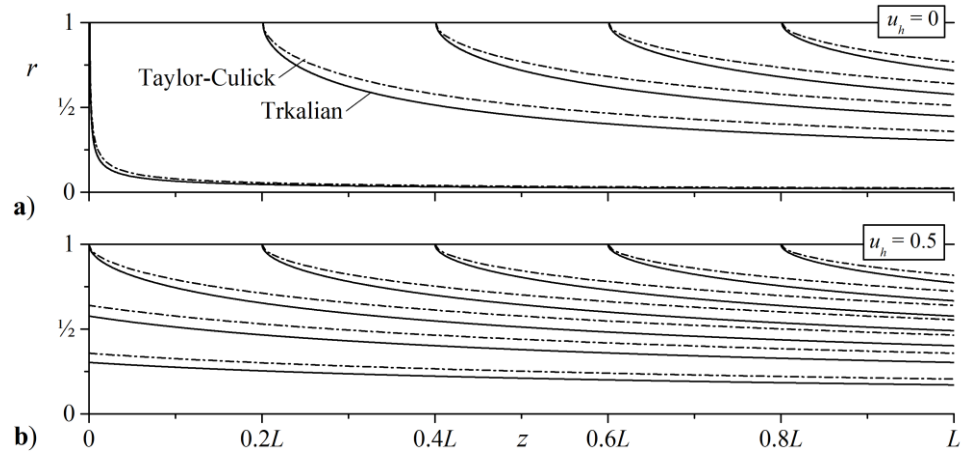


**Figure 4.1 Comparison between streamlines of the new solution and those corresponding to the Taylor-Culick solution for a simulated SRM.**

**a) Without and b) with headwall injection. This figure demonstrates the case of uniform burning at the headwall.**

Figure 4.1a,b for $u_h = 0$ and $0.5$. The second Beltramian solution is associated with a headwall injection velocity that simulates reactive flow in a solid rocket motor with a regressing propellant grain at the forward closure. Mass flow similarity is maintained by use of integral

$$\int_0^a \bar{u}_z (2\pi\bar{r})\mathrm{d}\bar{r} = \pi a^2 U_w \quad \text{or} \quad 2\pi u_h \int_0^1 \lambda_1 J_0(\lambda_1 r) J_1^{-1}(\lambda_1) r\mathrm{d}r = \pi \tag{4.5}$$

Which reveals $u_h = 0.5$, the same value that allows the similarity-conforming half-cosine to mimic reactive flow conditions in a TC configuration.[5]. It is valuable to note that the streamtube motion associated with the headwall injection profile becomes increasingly more pronounced as $u_h$ increases. Nevertheless, it is shown that the flow will always enter the chamber perpendicularly to the sidewall independent of the headwall injection speed. The figure also shows a representation of the TC streamlines, which are observed to exhibit faster flow turning than the new solution. The reason for the more rapid TC curvature may be attributed to its higher axial velocity and reduced radial velocity near the sidewall. In the case of the Trkalian and Beltramian solution, less severe velocity components at these locations lead to less pronounced flow turning. As expected the relatively sharp similarity patterns depicted in Figure

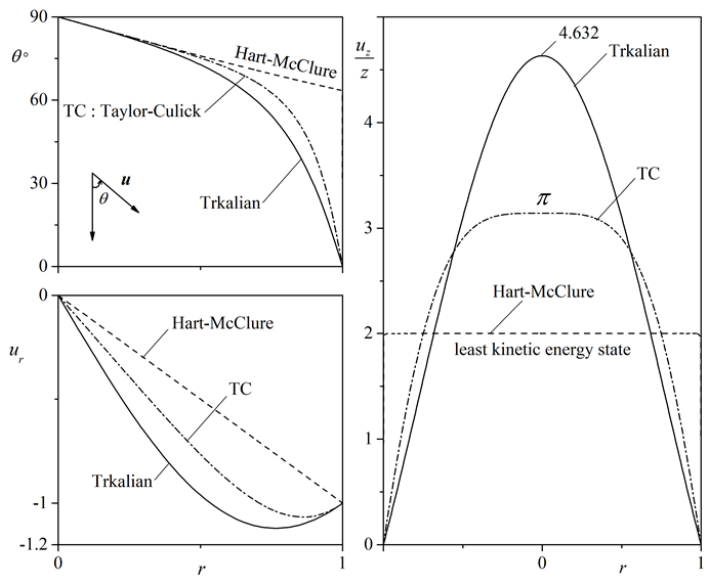


**Figure 4.2 Comparison between the Trkalian, Taylor-Culick, and Hart-McClure profiles. Results shown include a) the streamline turning angle, b) the radial velocity, and c) the axial velocity.**

4.2a are rapidly replaced by what is essentially streamtube motion when the headwall injection is incorporated, as seen in Figure 4.2b. Quantitatively, the flow turning angle $\theta$ may be defined as the slope of the local velocity as measured from the wall-normal direction, or $\theta(r) = (180/\pi)\tan^{-1}[-u_z/(zu_r)]$. This angle profile for the new solution is plotted in Fig. 4a alongside the TC flow turning angle and that of Hart-McClure (HM) profile. The HM profile corresponds to a potential mean flow profile, $\boldsymbol{u} = -r\boldsymbol{e}_r + 2z\boldsymbol{e}_z$, which was used by Hart and McClure (HM),[56] and other researchers, to model the bulk fluid motion in SRMs before the development of the classic TC solution.[57] An additional example of such use is documented in the work McClure, Hart and Cantrell.[58]. Further investigations of these profiles performed by Saad and Majdalani[33] demonstrate that the HM profile constitutes the state of least kinetic energy, which, unlike the present formulation, possess more energy than TC solution. In further assessing the flow turning parameter $\theta$ shown in Figure 4.2a, it is seen that the flow entering the chamber does indeed adhere to the no-slip requirement, as it has no parallel component at $r = 1$, where $\theta = 0^{\circ}$. Alternatively, the initiation of parallel flow motion at $r = 0$ may be identified in

the three cases where $\theta(0) = 90^{\circ}$. Interestingly, the HM motion is accompanied by a sudden variation in $\theta$ in the progression from sidewall to centerline. In the case of the TC and Trkalian models, the turn angle changes relatively slowly. As shown in work by Saad and Majdalani,[33] smoother gradients near the sidewall indicate a more energetic flow, which is typically accompanied by a more rapidly increasing radial velocity. These suggested trends are shown to be valid in Figure 4.2b and Figure 4.2c, in which the Trkalian flow exhibits the smoothest radial and axial velocities at any radial position.

In evaluating its radial velocity, the Trkalian $u_r$ is shown to achieve the highest peak velocities of the three profiles at a value of 1.121 (in absolute value), which is a 12.1% overshoot relative to the normalized sidewall injection speed. This overshoot peaks at radial location $r$ = 0.765, and is an expected occurrence, as it is required to compensate for the decreasing tubular area $(2\pi rL)$, which is observed in the normal direction to the incoming stream from the sidewalls. In the case of the TC solution, the radial velocity exhibits a 6.7% overshoot at $r$ = 0.861, which is approximately half as large, and occurs at a larger radius. In the case of the HM solution, $|u_r|$ decreases linearly from a value of unity at the wall to 0 at the centerline. This linear variation accompanies a similarly uniform axial velocity, as depicted in Fig. 5c., in which the axial velocities of the three solutions are compared, and show a steep HM model, a cosine-shaped TC velocity, and a Bessel-smooth Trkalian profile. As we evaluate closer to the centerline of the body, beyond the asymptotic velocity threshold of the TC profile, it is observed that the Trkalian field continues to increase, achieving a peak velocity of $u_z / z = 4.632$, which may be attributed to the need for $u_c$, the normalized injection velocity $(u_c = U_c / U_w)$ to accommodate mass conservation, which is given by $Q = 2\pi \int_0^1 u_z \, r \, \mathrm{d}r = 2\pi z$. As expected, the centerline speed of each model must resolve in a manner that preserves the total volumetric flow rate $Q$. While the lowest $u_c$ appears in the spatially uniform HM plug flow, the highest speed is achieved in the Trkalian profile, which exceeds the HM and TC models by values of 2.316 and 1.474, respectively. This increase in kinetic energy is, predictably, followed by a more rapid decrease in pressure along the centerline.

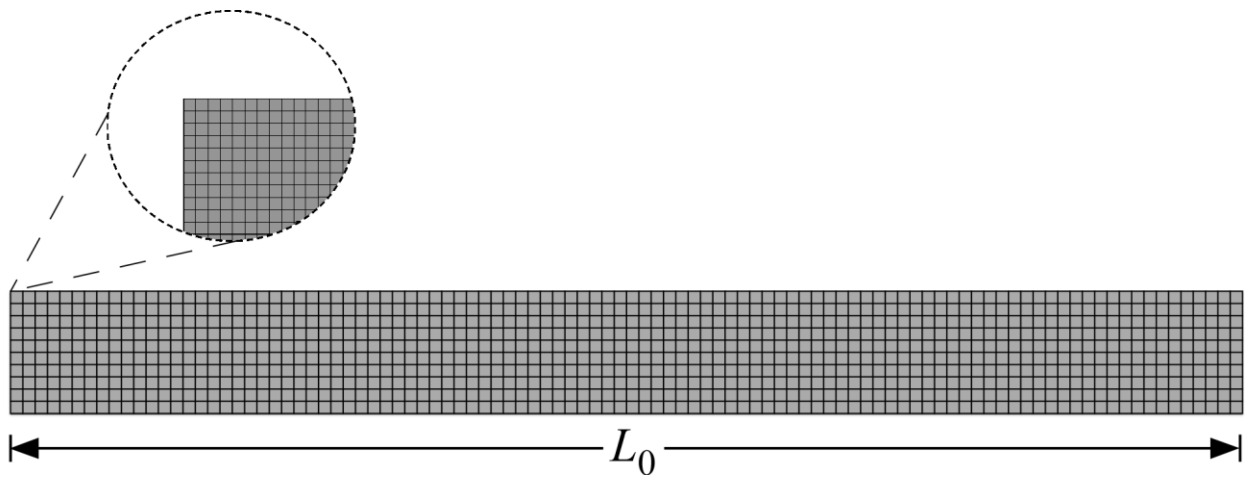


**Figure 4.3 Depiction of uniform mesh structure utilized in CFD analysis**

## 4.3 Numerical Verification of Exact Solution

The flow field construct presented above, namely that of an inviscid solution with an inert headwall injection profile (i.e. Eqs. (3.20) and (4.2)) is confirmed via numerical verification. The tool utilized is a pressure-based, finite volume solver (FLUENT™) with a two dimensional axisymmetric format that accommodates swirl velocity, and a structured cylindrical mesh, with a schematic presented in Figure 4.3. By utilizing the velocity component functions, a solution boundary that incorporates velocity inlet flow injection at the headwall and sidewall and an initialization field for the rest of the fluid volume, convergence is demonstrated across the field, with variances between analytic and numerical solutions typically less than 0.4%. Naturally, as the solution is developed to accommodate a cylinder of infinite length, a small degree of boundary condition reflection is present, but constrained within the aft 10-20% of a given solution field. The numerical demonstration incorporated a cylinder with radius and length of 1m x 8m (for an aspect ratio of $L = 8$) for the area of interest, with a total length of 10m to accommodate the described pressure outlet boundary limitations and to serve as a far field plenum. The mesh incorporated approximately 384,000 cells in total, and utilized an accompanying 110,000 point initialization field with resolution enhancement at the wall boundaries. A least-squares regression method accommodated interpolation of the initial field via

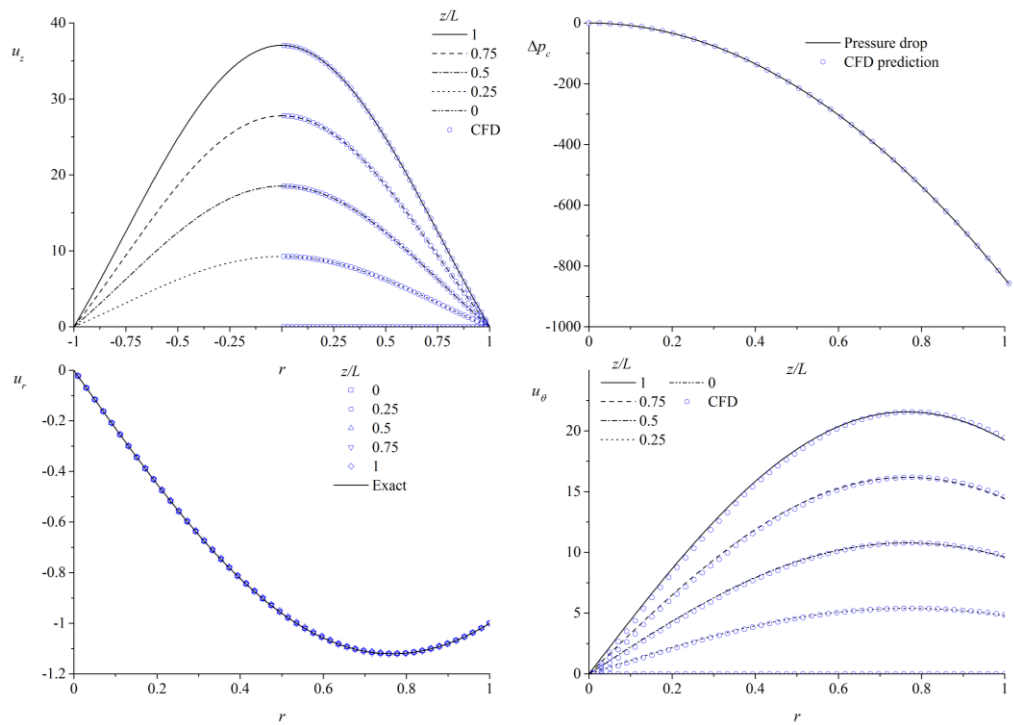


**Figure 4.4 Demonstration of agreement between CFD (circles) and analytical solutions (lines) of the proposed flowfield**

the tool. The SIMPLE scheme was used to calculate pressure and velocity, while a third order upwind method accounted for spatial discretization.

The results for an initial wall velocity of $u = 10\ m/s$ are presented in Figure 4.4, with comparison made between analytical and numerical solutions for component velocity and pressure, and demonstrating agreement across the field. Velocity profiles in each component direction are shown at various axial stations, while centerline pressure profile agreement is also demonstrated. This exercise brings additional confidence to the methods utilized, as it demonstrates that the analytical methods constructed are sufficiently satisfying the concepts of continuity and momentum conservation, as evidenced by its convergence in the inviscid CFD solution.

## 4.4 Flowfield Development Conclusions

In arriving at this step in the study, the Bragg-Hawthorne equation and the problem-defining boundary conditions were manipulated to demonstrate that both the historic Taylor-Culick field, as well as a new, swirl-generating field, can be developed, with the key differentiator in the process being the selection of a relation between the streamfunction, the stagnation head, and angular momentum. The selection utilized in the new solution is supported in literature[54]. By way of comparison to the Taylor-Culick formulation, where tangential motion is restricted during the construction of the solution, the angular momentum associated with new solution is granted the freedom to change with the stream function, and this property enables the derivation of a similarity solution with three non-vanishing velocity components. In this frictionless, inviscid environment, it may be helpful to note that the salient flow features compare favorably with their Taylor-Culick counterparts, notwithstanding their dissimilar origins. Minor differences between the two solutions are observed when considering their minimum radial and maximum axial velocities, vorticities, and pressure distributions. The primary advantage of the Beltramian profile may be attributed to its higher kinetic energy, tangential velocity exhibiting a physically-plausible axial dependence, and its finite vorticity in all three spatial directions. These elements are corroborated by various laboratory and computational experiments, where the inevitable evolution of swirl appears to be imminent, especially in long cylindrical chambers comprising constant circular cross-sections. Finally, the work to this point is further validated by the use of a computational fluid dynamics tool to demonstrate that the resulting velocity profiles do indeed conform continuously to the relevant first principles of the conservation of mass, and linear and angular momentum.

Regarding the centerline singularity of the swirl velocity, or its inability to observe the no-slip condition at the sidewall, these effects are both consequences of the flow being inviscid. These defects may be overcome using the tools of perturbation theory, where the presence of a core and sidewall boundary layers in the tangential direction must be accounted for. This correction factor, outside the scope of this text, has been developed and presented to the community[49] with related future work to be described in Chapter 7.

# Chapter 5

# Lagrangian Optimization of the Flowfield

This chapter utilizes the newly-developed Beltramian flow field to develop and describe optimized forms of the solution that will yield maximum or minimum kinetic energy, while still satisfying the original boundary conditions and relations identified in the flow field construction. The introduction of an energy-based approximation for sufficiently long chambers is also introduced to further generalize the flowfields. As this research has been well communicated to the community over the course of its development, the methods presented in the subsections of this chapter have been previously published by the author and his advisor, and with the support of Dr. Tony Saad who has studied these optimization methods on the Taylor-Culick solution[49-51].

## 5.1 Problem Definition

In the previous chapters, it was demonstrated that the classic Taylor-Culick mean flow may be recovered from a partial solution of the Bragg-Hawthorne equation (BHE), and that another new and interesting solution may also be developed via the construct. This new solution contemplated is shown to be of the *Trkalian* type, meaning that it exhibits velocities and vorticities that are globally parallel. Additionally, while the original Taylor-Culick (TC) streamfunction,[1] is manifested in a sinusoidal nature, the new model possesses a Bessel function representation. These representations lend themselves well to an evaluation of other energy-

optimized solutions of similar form that also satisfy the initial constraints. Saad and Majdalani's[33] process, which is utilized their work studying Taylor-Culick bulk fluid motion in solid and hybrid rocket motors,[32, 33, 59, 60] and bidirectional vortex motions[61, 62], form the basis of this study.

## 5.2 Formulation of Solutions from the Bragg-Hawthorne Equation

The previous chapters describe the development of the swirl-augmented profile, and its relation to the classic Taylor-Culick solution. To recap, both the new solution and the Taylor-Culick model may be retrieved from the Bragg-Hawthorne equation, which relates the vorticity transport equation, the streamfunction $\psi$, the fluid head $\bar{H} = \bar{p}/\bar{\rho} + \frac{1}{2}\bar{\boldsymbol{u}}\cdot\bar{\boldsymbol{u}}$, and the angular momentum $\bar{B} = \bar{r}\bar{u}_\theta$, into one PDE via:

$$\frac{\partial^2\bar{\psi}}{\partial\bar{r}^2} - \frac{1}{\bar{r}}\frac{\partial\bar{\psi}}{\partial\bar{r}} + \frac{\partial^2\bar{\psi}}{\partial\bar{z}^2} = \bar{r}^2\frac{\mathrm{d}\bar{H}}{\mathrm{d}\bar{\psi}} - \bar{B}\frac{\mathrm{d}\bar{B}}{\mathrm{d}\bar{\psi}} \tag{5.1}$$

Or non-dimensionally, with $B = ru_\theta$ and $H = p/\rho + \frac{1}{2}\boldsymbol{u}\cdot\boldsymbol{u}$, we have

$$\frac{\partial^2\psi}{\partial r^2} - \frac{1}{r}\frac{\partial\psi}{\partial r} + \frac{\partial^2\psi}{\partial z^2} = r^2\frac{\mathrm{d}H}{\mathrm{d}\psi} - B\frac{\mathrm{d}B}{\mathrm{d}\psi} \tag{5.2}$$

It was shown previously that selection of the terms

$$B = 0 \text{ and } \frac{\mathrm{d}H}{\mathrm{d}\psi} = -\mathcal{C}^2\psi \text{ or } H(\psi) = -\tfrac{1}{2}\mathcal{C}^2\psi^2 + H_0 \tag{5.3}$$

will return the non-swirling Taylor-Culick streamfunction and velocity profiles, shown to be

$$\psi = z\sin(\tfrac{1}{2}\pi r^2); \quad \boldsymbol{\Omega} = \pi^2 zr\sin(\tfrac{1}{2}\pi r^2)\boldsymbol{e}_\theta; \quad \boldsymbol{u} = -r^{-1}\sin(\tfrac{1}{2}\pi r^2)\boldsymbol{e}_r + \pi z\cos(\tfrac{1}{2}\pi r^2)\boldsymbol{e}_z \tag{5.4}$$

It was also shown that an alternative selection of constraints on the stagnation head and angular momentum, namely

$$B\frac{\mathrm{d}B}{\mathrm{d}\psi} = \mathcal{C}^2\psi \text{ and } \frac{\mathrm{d}H}{\mathrm{d}\psi} = 0 \text{ or } H(\psi) = H_0 = \text{const.} \tag{5.5}$$

will produce a new, swirl-promoting flowfield, which is manifested from the first partial eigensolution of the Bragg-Hawthorne Equation. In the case of an inert headwall, the profile may be described as:

$$\psi(r,z) = rz\frac{J_1(\lambda_1 r)}{J_1(\lambda_1)} \tag{5.6}$$

$$\boldsymbol{u} = -\frac{J_1(\lambda_1 r)}{J_1(\lambda_1)}\boldsymbol{e}_r + \frac{\lambda_1 z J_1(\lambda_1 r)}{J_1}\boldsymbol{e}_\theta + \frac{\lambda_1 z J_0(\lambda_1 r)}{J_1}\boldsymbol{e}_z \tag{5.7}$$

$$\boldsymbol{\Omega} = -\frac{\lambda_1 J_1(\lambda_1 r)}{J_1(\lambda_1)}\boldsymbol{e}_r + \frac{\lambda_1^2 z J_1(\lambda_1 r)}{J_1(\lambda_1)}\boldsymbol{e}_\theta + \frac{\lambda_1^2 z J_0(\lambda_1 r)}{J_1(\lambda_1)}\boldsymbol{e}_z \tag{5.8}$$

$$\begin{aligned}\Delta p = p - p_0 &= \frac{J_1^2(\lambda_1 r) - z^2\lambda_1^2\left[J_0^2(\lambda_1 r) + J_1^2(\lambda_1 r)\right]}{2J_1^2(\lambda_1)} \\ &\approx -1.85519 J_1^2(\lambda_1 r) - 10.729 z^2\left[J_0^2(\lambda_1 r) + J_1^2(\lambda_1 r)\right]\end{aligned} \tag{5.9}$$

where $\lambda_1$ represents to the first root of the zeroth-order Bessel function of the first kind, $\lambda_1 \cong 2.40483$. From this starting point, we may now study the remainder of the eigensolutions, and optimize to produce solutions of similar form that both satisfy the initial constraints and also demonstrate the maximum and minimum possible kinetic energy.

## 5.3 Solution Development Via Eigenfunction Expansion

As described in Chapter 3, the streamfunction solution may be generally identified as $\psi(r,z) = r(\alpha z + \beta)J_1(Cr)$, which is based on the first eigensolution, and ultimately leads to Eqs. (5.6), (5.7), and (5.8). However, because of the linear nature of the solution, it is possible to generalize the solution further by constructing a summation of all eigenfunctions. To begin we evaluate the eigencondition that constrains the axial velocity at the sidewall, $u_z(1,z) = 0$, which creates the no-slip requirement. This eigencondition is met for any of the following values of $\mathcal{C}$, which are all roots of the zeroth-order Bessel Function of the first kind, namely

$$\mathcal{C} = \lambda_n = j_{0,n} = \{2.40483, 5.52008, 8.65373...\} \text{ for } n = 1,2,3,... \tag{5.10}$$

When we recall that all solutions (and summations) that satisfy the eigencondition can be valid, we can generalize the streamfunction by summing over all eigensolutions, writing

$$\psi(r,z) = \sum_{n=1}^{\infty}\psi_n = \sum_{n=1}^{\infty} r(\alpha_n z + \beta_n)J_1(\lambda_n r) \tag{5.11}$$

With this new form of $\psi(r,z)$ in hand, we may now re-evaluate each of the initial constraints in Eq. (2.4), with the consideration that each constraint may be written as a derivative of $\psi(r,z)$. Starting with the sidewall velocity requirement, we now have:

$$u_r(1,z) = -\frac{\partial\psi(1,z)}{\partial z} = -\sum_{n=1}^{\infty}\alpha_n J_1(\lambda_n) = -1 \tag{5.12}$$

and the resulting key equality,

$$\sum_{n=1}^{\infty}\alpha_n J_1(\lambda_n) - 1 = 0 \tag{5.13}$$

emerges as the fundamental constraint that will be used in conjunction with a Lagrangian optimization technique for the purpose of maximizing or minimizing the flow's total kinetic energy.

Our next physical requirement consists of the headwall injection selection which, for the case of an inert wall, returns

$$u_z(r,0) = \frac{1}{r}\frac{\partial\psi(r,0)}{\partial r} = \sum_{n=1}^{\infty}\lambda_n\beta_n J_0(\lambda_n r) = 0 \quad \text{or} \quad \beta_n = 0 \tag{5.14}$$

Which as a result, Eq. (5.11) reduces to

$$\psi(r,z) = \sum_{n=1}^{\infty}\alpha_n r z J_1(\lambda_n r) \tag{5.15}$$

With this more simplified form, the boundary condition that constrains swirl at the headwall may be used to develop an expanded function for the tangential velocity. Given that

$$u_{\theta,n} = \frac{1}{r}\sqrt{\mathcal{C}_n^2\psi_n^2 + \mathcal{D}_n} = \frac{1}{r}\sqrt{\lambda_n^2\alpha_n^2 r^2 z^2 J_1^2(\lambda_n r) + \mathcal{D}_n} \tag{5.16}$$

the limit at the centerline produces

$$u_{\theta,n}(0,0) = \lim_{r\to 0}\frac{1}{r}\sqrt{\lambda_n^2\alpha_n^2 r^2 z^2 J_1^2(\lambda_n r) + \mathcal{D}_n} = 0 \quad \text{and so} \quad \mathcal{D}_n = 0 \tag{5.17}$$

We are now left with

$$u_{\theta,n} = \alpha_n\lambda_n z J_1(\lambda_n r) \tag{5.18}$$

The final result is a new set of streamfunction and flow velocity equations that both satisfy the fundamental eigenconditions and a re-application of the boundary conditions, namely

$$\psi(r,z)=\sum_{n=1}^{\infty}\alpha_n r z J_1(\lambda_n r) \tag{5.19}$$

$$u_r=\sum_{n=1}^{\infty}u_{r,n}=-\sum_{n=1}^{\infty}\alpha_n J_1(\lambda_n r) \tag{5.20}$$

$$u_\theta=\sum_{n=1}^{\infty}u_{\theta,n}=\sum_{n=1}^{\infty}\alpha_n\lambda_n z J_1(\lambda_n r) \tag{5.21}$$

$$u_z=\sum_{n=1}^{\infty}u_{z,n}=\sum_{n=1}^{\infty}\alpha_n\lambda_n z J_0(\lambda_n r) \tag{5.22}$$

## 5.4 Kinetic Energy Optimization

To seek out optimized solutions with maximum or minimum energy content, a properly formed description of total kinetic energy is required. We may begin with a description of local kinetic energy for each eigensolution, written as

$$E_n(r,\theta,z)=\tfrac{1}{2}u_n^2=\tfrac{1}{2}(u_{r,n}^2+u_{\theta,n}^2+u_{z,n}^2) \tag{5.23}$$

where the flow velocity components are described by Eqs. (5.20), (5.21), and (5.22). In order to assess the kinetic energy over the entire domain, a summation of linearly independent eigensolutions with individual kinetic energies can be assumed, which then allows a volume integration across the domain, via

$$E_\nu(r,\theta,z)=\frac{1}{2}\sum_{n=1}^{\infty}\int_0^{2\pi}\int_0^{L}\int_0^{1}(u_{r,n}^2+u_{\theta,n}^2+u_{z,n}^2)r\mathrm{d}r\mathrm{d}z\mathrm{d}\theta$$

$$=\frac{1}{2}\sum_{n=1}^{\infty}\int_0^{2\pi}\int_0^{L}\int_0^{1}[\alpha_n^2J_1^2(\lambda_n r)+\alpha_n^2\lambda_n^2z^2J_1^2(\lambda_n r)+\alpha_n^2\lambda_n^2z^2J_0^2(\lambda_n r)]\ r\mathrm{d}r\mathrm{d}z\mathrm{d}\theta \tag{5.24}$$

where the notation $J_n^a(b)=[J_n(b)]^a$ is used. By factoring out the injection constant, we retrieve

$$E_\nu(r,\theta,z)=\tfrac{1}{2}\sum_{n=1}^{\infty}\int_0^{2\pi}\int_0^{L}\int_0^{1}\alpha_n^2[J_1^2(\lambda_n r)+\lambda_n^2z^2J_1^2(\lambda_n r)+\lambda_n^2zJ_0^2(\lambda_n r)]r\mathrm{d}r\mathrm{d}z\mathrm{d}\theta \tag{5.25}$$

The volume integral may then be evaluated to produce

$$E_\nu=\frac{\pi L}{6}\sum_{n=1}^{\infty}\frac{\alpha_n^2}{\lambda_n}[\lambda_n^2(3+L^2\lambda_n^2)J_0^2(\lambda_n)-2(3+L^2\lambda_n^2)J_0(\lambda_n)J_1(\lambda_n)+\lambda_n(3+2L^2\lambda_n^2)J_1^2(\lambda_n)]\,. \tag{5.26}$$

Because we recall that $J_0(\lambda_n) = 0$, the volume integral is further simplified into

$$E_v = \tfrac{1}{6}\pi L \sum_{n=1}^{\infty} \alpha_n^2 (2L^2\lambda_n^2 + 3) J_1^2(\lambda_n) \tag{5.27}$$

which may be rearranged to reflect a volume-dependent quantity. Factoring out two spatial dimensions in $L^2$, we produce

$$E_v = \tfrac{1}{6}\pi L^3 \sum_{n=1}^{\infty} [2\alpha_n^2\lambda_n^2 J_1^2(\lambda_n) + 3L^{-2}\alpha_n^2 J_1^2(\lambda_n)] = \tfrac{1}{6}\pi L^3 \sum_{n=1}^{\infty} \alpha_n^2 (L^{-2}a_n + d_n) \tag{5.28}$$

where

$$a_n = 3J_1^2(\lambda_n); \quad d_n = 2\lambda_n^2 J_1^2\left(\lambda_n\right) \tag{5.29}$$

We have now identified the three elements that are required for the application of the Lagrangian optimization technique:

- the quantity under consideration for optimization $\left(E_v\right)$,
- the undetermined sidewall injection coefficient $\left(\alpha_n\right)$, and
- the fundamental constraint relation given by Eq. (5.13).

It is apparent from evaluation of $\left(E_v\right)$ that the total kinetic energy content for this solution is driven by both the system's geometric aspect ratio $L$ and the undefined coefficient $\alpha_n$. As a result, we may define a constrained energy function $G$ as a consolidated relation, which incorporates the volume energy equation and the fundamental constraint. Then, via the Lagrangian multiplier method, we are able to identify the zero gradient point of $G$ that will produce an energy-optimized value for $\alpha_n$. The constrained energy equation may be written as

$$G(\alpha_n, \chi) = E_v + \chi[\sum_{n=1}^{\infty} \alpha_n J_1(\lambda_n) - 1] \tag{5.30}$$

where $\chi$ is a new, presently undefined Lagrangian multiplier. Note that when the infinite sum vanishes, Eq. (5.30) returns $G = E_v$ for all $\chi$. At this stage, a gradient operation may be performed on $G$, with the objective of determining its zero gradient point. We now write

$$\nabla G(\alpha_n, \chi) = 0, \qquad n = \{1, 2, ..., \infty\} \tag{5.31}$$

In which each term must be evaluated one at a time. For example, one must take

$$\frac{\partial G}{\partial \chi} = \sum_{n=1}^{\infty} \alpha_n J_1(\lambda_n) - 1 = 0 \tag{5.32}$$

in concert with

$$\frac{\partial G}{\partial \alpha_n} = \tfrac{1}{3}\pi L^3 \alpha_n (L^{-2} a_n + d_n) + \chi J_1(\lambda_n) = 0 \tag{5.33}$$

with the resulting combination returning

$$\alpha_n = -\frac{3}{\pi L^3} \frac{\chi}{(3L^{-2} + 2\lambda_n^2) J_1(\lambda_n)} \tag{5.34}$$

It is clear that Eq. (5.34) provides the necessary linkage between the undefined coefficient $\chi$ responsible for the volume-based kinetic energy content and the fundamental constraint $\alpha_n$, which is now expressible in terms of $\chi$. The resulting connection may be utilized by replacing $\alpha_n$ in Eq. (5.33) with its corresponding value in Eq. (5.34). Note that the $J_1(\lambda_n)$ terms cancel identically, hence leaving us with

$$\frac{\partial G}{\partial \chi} = -\frac{3\chi}{\pi L^3} \sum_{n=1}^{\infty} \frac{1}{(3L^{-2} + 2\lambda_n^2)} - 1 = 0 \tag{5.35}$$

This relation enables us to rearrange terms and simplify $\chi$ via

$$\chi = -\frac{\pi L^3}{3} \frac{1}{\sum_{n=1}^{\infty} (3L^{-2} + 2\lambda_n^2)^{-1}} = -\frac{\pi L^3}{3K}; \quad K \equiv \sum_{i=1}^{\infty} (3L^{-2} + 2\lambda_i^2)^{-1} \tag{5.36}$$

Inserting this new description of $\chi$ back into $\alpha_n$ provides

$$\alpha_n = -\frac{3}{\pi L^3} \frac{1}{(3L^{-2} + 2\lambda_n^2) J_1(\lambda_n)} \left( -\frac{\pi L^3}{3K} \right) = \frac{1}{(3L^{-2} + 2\lambda_n^2) J_1(\lambda_n) K} \tag{5.37}$$

At this point, we have arrived as a closed form of $\alpha_n$, which may then be optimized based on kinetic energy content in a manner consistent with the fundamental constraint. When incorporated into the volume kinetic energy formula (Eq. (5.28)), we may recover

$$E_v = \frac{\pi L^3}{6} \sum_{n=1}^{\infty} \frac{1}{(2\lambda_n^2 + 3L^{-2}) K^2} \tag{5.38}$$

## 5.5 Large L Approximation for Slender Bodies

In assessing the variation of the energy content relative to chamber aspect ratio, a method of simplification may be achieved by studying the variation of $E_\nu$ with increasing values of $L$, with the intent of verifying that energy content converges as $L$ becomes large. This assumption is typically made in the modeling of long chambers associated with solid rocket motors. We may for the sake of simplicity utilize the relation

$$\varepsilon = \frac{E_\nu}{L^3} = \frac{\pi}{6}\sum_{n=1}^{\infty}\frac{1}{(2\lambda_n^2 + 3L^{-2})K^2} \text{ where } K = \sum_{i=1}^{\infty}(3L^{-2} + 2\lambda_i^2)^{-1} \tag{5.39}$$

A study of Eq. (5.39) reveals that the $L^{-2}$ terms will rapidly vanish as $L$ becomes large. Additionally, evaluating $K$ at large $L$ produces an interesting result that will be leveraged in the remainder of the analysis.

$$\lim_{L\to\infty} K = \sum_{i=1}^{\infty}(3L^{-2} + 2\lambda_i^2)^{-1} = \sum_{i=1}^{\infty}(2\lambda_i^2)^{-1} \tag{5.40}$$

Because $\lambda_i$ represents the $i^{\text{th}}$ root of the zeroth order Bessel function of the first kind, further evaluation of this sum leads to the following interesting simplification:

$$\sum_{i=1}^{\infty}(\lambda_i^2)^{-1} = \sum_{i=1}^{\infty}[(j_{0,i})^{-2}] = \frac{1}{4} \tag{5.41}$$

$$K_\infty = \lim_{L\to\infty} K = \sum_{i=1}^{\infty}(3L^{-2} + 2\lambda_i^2)^{-1} = \sum_{i=1}^{\infty}(2\lambda_i^2)^{-1} = \frac{1}{8} \tag{5.42}$$

This element is noted as particularly interesting because a seemingly irrational set of Bessel function roots, when summed in the manner prescribed by Eq. (5.41), produce to a rational result, provided that they are evaluated to a sufficiently large value of $i$. This result, and a discussion of similar summations is provided by Sneddon[63]. With the development of these approximations for a large $L$ solution, their values may be substituted back into the energy density relation to produce a suitable formulation for elongated porous chambers where one may safely use

$$\varepsilon_\infty = \lim_{L\to\infty}\frac{E_\nu}{L^3} = \frac{\pi}{6}\sum_{n=1}^{\infty}\frac{1}{(2\lambda_n^2)K^2} = \frac{\pi}{6}\sum_{n=1}^{\infty}\frac{32}{\lambda_n^2} = \frac{16\pi}{3}\sum_{n=1}^{\infty}\lambda_n^{-2} = \frac{16\pi}{3}\left(\frac{1}{4}\right) = \frac{4\pi}{3} \tag{5.43}$$

and

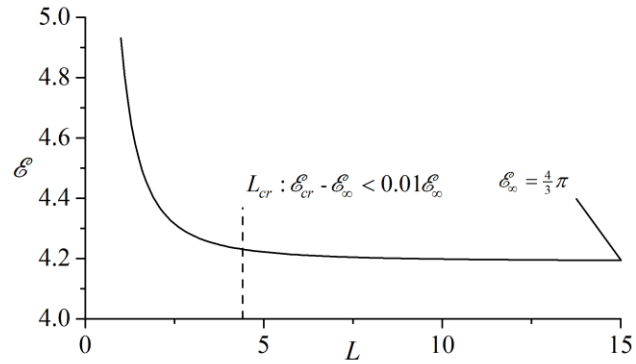


**Figure 5.1 Depiction of the variation in energy density with increasing length, and demonstration of critical length concept.**

$$\alpha_{n,\infty} = \lim_{L\to\infty} \alpha_n = \frac{4}{\lambda_n^2 J_1(\lambda_n)} \tag{5.44}$$

Two elements of this result should be highlighted. First, the interesting result of Eq. (5.42) presents itself again in Eq. (5.43), where it contributes to reducing the infinite sum to a simple constant. Second, the determined value of $\varepsilon_\infty$ is shown to be twice that of its counterpart in the similar analysis performed on the non-swirling Taylor-Culick profile by Saad and Majdalani.[33] Quite interestingly, it may be confirmed that the energy densities of both models become identical when the contribution of the swirl velocity is discounted in the present formulation.

We may now from this point utilize our simplified $\alpha_n$ at large values of $L$ in order to simplify the streamfunction and flow velocity equations for slender cases with length ratios exceeding a critical value, $L_{cr}$, beyond which the energy density does not vary from $\varepsilon_\infty$ by more than 1%. By numerically evaluating this condition, we are able to identify a critical aspect ratio of $L_{cr} \approx 4.415$, as depicted in Figure 5.1. This simplification is not particularly restrictive, because most rocket motors and porous chambers of interest have much larger aspect ratios, generally between 5 and 50, with an average around 20[64].

## 5.6 Generalization of Energy Optimized Solution

While the Lagrangian optimization method does indeed develop an energy optimized formulation, it is not possible to identify in advance if the result corresponds to a maximum- or a minimum-energy solution. Based on the effort of Majdalani and Saad,[59] it is plausible that two families of solutions exist, with varying energy levels as expected, and from which the original model may be recovered as a special case. To begin, we will assume that the chamber length is greater than $L_{cr} \approx 4.415$ so that Eq. (5.44) may be used to provide for a more simplified framework.

In the evaluation of Eq. (5.44), we may follow the path of Saad and Majdalani[33] by hypothesizing that a link exists between the integer constant and the power associated with the Bessel root, which appears in the denominator. This would be conveyed as

$$\alpha_n\big|_{L\to\infty} \approx \frac{4}{\lambda_n^2 J_1(\lambda_n)} \longrightarrow \frac{A_q}{\lambda_n^q J_1(\lambda_n)} \tag{5.45}$$

$$\alpha_n^-(q) = \frac{A_q}{\lambda_n^q J_1(\lambda_n)}, \;\; q \geq 2 \tag{5.46}$$

where $q = 2$ represents the state of least kinetic energy, and solutions corresponding to $q > 2$ will possess higher kinetic energies that will approach an asymptotic limit. This relation may be evaluated against the sidewall injection sequence, which controls the development of the original streamfunction solution, to provide:

$$-\sum_{n=1}^{\infty} J_1(\lambda_n)\;\alpha_n(q) = -1; \quad q \geq 2 \tag{5.47}$$

and so

$$\sum_{n=1}^{\infty} J_1(\lambda_n)\;\frac{A_q}{\lambda_n^q J_1(\lambda_n)} = 1; \quad q \geq 2 \quad \text{or} \quad \sum_{n=1}^{\infty} \frac{A_q}{\lambda_n^q} = 1\,,\; q \geq 2 \tag{5.48}$$

We may then re-write $A_q$ as

$$A_q = \frac{1}{\sum_{n=1}^{\infty} \lambda_n^{-q}}\;; \quad q \geq 2 \tag{5.49}$$

Now that a finite term for $A_q$ has been identified, it may be re-inserted into Eq. (5.46) to produce

$$\alpha_n^-(q) = \frac{1}{\lambda_n^q J_1(\lambda_n)\sum_{i=1}^{\infty}\lambda_i^{-q}}; \quad q \geq 2 \tag{5.50}$$

This proposed coefficient can be verified to be valid for several values of $q$; Indeed, this may be tested against the revised sidewall injection sequence in Eq. (5.47). For example, using $q = 2$, we obtain:

$$\sum_{n=1}^{\infty} -\alpha_n^-(2) J_1(\lambda_n) = -1 \quad \text{or} \quad \sum_{n=1}^{\infty} -\frac{1}{\lambda_n^2 J_1(\lambda_n)\sum_{n=1}^{\infty}\lambda_n^{-2}} J_1(\lambda_n) = -1 \tag{5.51}$$

This is so because

$$\sum_{n=1}^{\infty}\frac{1}{\lambda_n^2\sum_{i=1}^{\infty}\lambda_i^{-2}} = 1; \quad \sum_{n=1}^{\infty}\frac{1}{\lambda_n^2\left(\frac{1}{4}\right)} = 1; \quad 4\sum_{n=1}^{\infty}\frac{1}{\lambda_n^2} = 1; \quad \text{or} \quad 4\left(\frac{1}{4}\right) = 1 \tag{5.52}$$

It is apparent that the recursive nature of this formulation enables us to confirm that for $q \geq 2$, the proposed coefficient will satisfy the sidewall injection sequence, and by extension the forms developed for the streamfunction, velocity, and vorticity. Because the construction method shares similarity with a similar effort with the TC solution in Saad and Majdalani,[33] the generic coefficient will be now be associated with a similarly-named "Type I" family of solutions.

Beyond the Type I coefficient, it is possible to hypothesize an alternative "Type II" coefficient that also satisfies the boundary conditions and flowfield, but will otherwise result in a significantly different effect on the velocity development and associated kinetic energy generation. In this case, we will evaluate an alternate construct from that in Eq. (5.45) by introducing a "conjugate" coefficient

$$\alpha_n\big|_{L\to\infty} \approx \frac{4}{\lambda_n^2 J_1(\lambda_n)} \longrightarrow \frac{B_q}{\lambda_n^q} \tag{5.53}$$

which translates into

$$\alpha_n^+(q) = \frac{B_q}{\lambda_n^q}; \quad q \geq 2 \tag{5.54}$$

**Table 1 Flowfield solutions resulting from the generalization procedure.**

| Original Solution | Type I Solution | Type II Solution |
|---|---|---|
| $\alpha_n = \dfrac{4}{\lambda_n^2 J_1(\lambda_n)}$ | $\alpha_n^-(q) = \dfrac{1}{\lambda_n^q J_1(\lambda_n)\sum_{i=1}^{\infty}\lambda_i^{-q}},\ q \geq 2$ | $\alpha_n^+(q) = \dfrac{1}{\lambda_n^q \sum_{i=1}^{\infty} J_1(\lambda_i)\lambda_i^{-q}},\ q \geq 2$ |
| $\psi(r,z) = \sum_{n=1}^{\infty}\alpha_n r z J_1(\lambda_n r)$ | $\psi(r,z,q) = \sum_{n=1}^{\infty}\alpha_n^-(q) r z J_1(\lambda_n r)$ | $\psi(r,z,q) = \sum_{n=1}^{\infty}\alpha_n^+(q) r z J_1(\lambda_n r)$ |
| $u_r(r) = \sum_{n=1}^{\infty} -\alpha_n J_1(\lambda_n r)$ | $u_r(r,q) = \sum_{n=1}^{\infty} -\alpha_n^-(q) J_1(\lambda_n r)$ | $u_r(r,q) = \sum_{n=1}^{\infty} -\alpha_n^+(q) J_1(\lambda_n r)$ |
| $u_\theta(r,z) = \sum_{n=1}^{\infty}\alpha_n \lambda_n z J_1(\lambda_n r)$ | $u_\theta(r,z,q) = \sum_{n=1}^{\infty}\alpha_n^-(q)\lambda_n z J_1(\lambda_n r)$ | $u_\theta(r,z,q) = \sum_{n=1}^{\infty}\alpha_n^+(q)\lambda_n z J_1(\lambda_n r)$ |
| $u_z(r,z) = \sum_{n=1}^{\infty}\alpha_n \lambda_n z J_0(\lambda_n r)$ | $u_z(r,z,q) = \sum_{n=1}^{\infty}\alpha_n^-(q)\lambda_n z J_0(\lambda_n r)$ | $u_z(r,z,q) = \sum_{n=1}^{\infty}\alpha_n^+(q)\lambda_n z J_0(\lambda_n r)$ |

where $q = 2$ can be shown to represent a state of maximum kinetic energy. As before, this relationship may be inserted into the sidewall injection sequence to produce:

$$B_q = \frac{1}{\sum_{i=1}^{\infty} J_1(\lambda_i)\lambda_i^{-q}}; \quad q \geq 2 \tag{5.55}$$

$$\alpha_n^+(q) = \frac{1}{\lambda_n^q \sum_{i=1}^{\infty} J_1(\lambda_i)\lambda_i^{-q}}; \quad q \geq 2 \tag{5.56}$$

Again we may verify the legitimacy of this result by trying, with $q = 2$, to satisfy the fundamental constraint via

$$\sum_{n=1}^{\infty} -\alpha_n^+(2) J_1(\lambda_n) = -1 \rightarrow \sum_{n=1}^{\infty} \frac{1}{\lambda_n^2 \sum_{i=1}^{\infty} J_1(\lambda_i)\lambda_i^{-2}} J_1(\lambda_n) = 1 \rightarrow \sum_{n=1}^{\infty} J_1(\lambda_n)\lambda_n^{-2} \frac{1}{\sum_{i=1}^{\infty} J_1(\lambda_i)\lambda_i^{-2}} = 1 \tag{5.57}$$

With the two generalized solutions now confirmed to satisfy the original constraint, the resulting streamfunctions and velocities can be compared to the original solution, as described in Table 1. In addition, the variation of component flow velocities across their respective dimensions of the volume is illustrated in Figure 5.2.

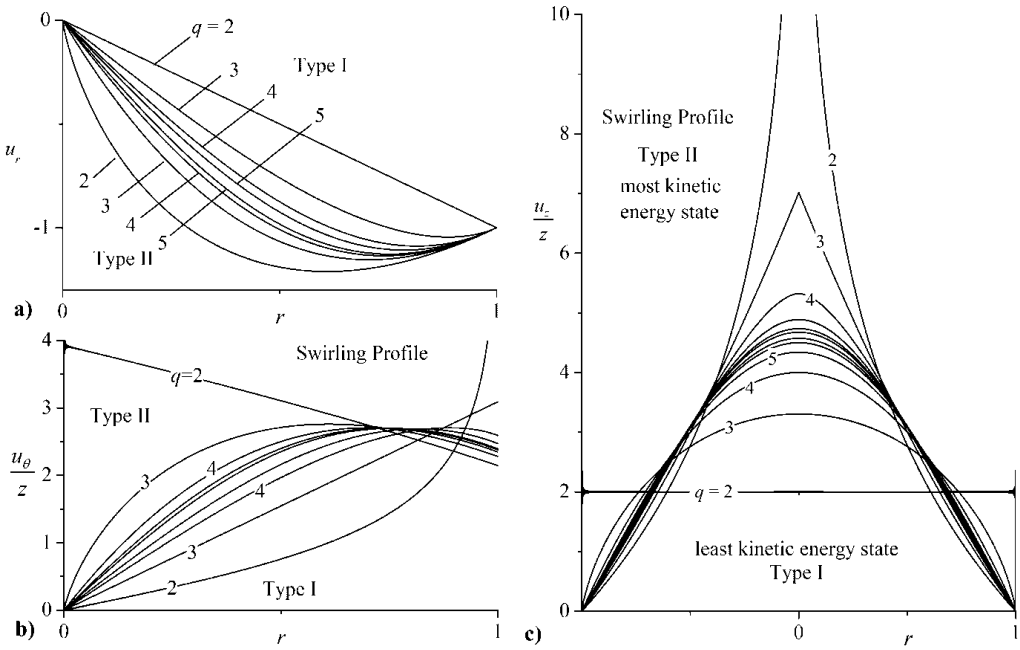


**Figure 5.2 Variation of velocity distributions across the volume radius with increasing values of $q$.**

In evaluating the effect of increasing $q$, it is apparent that the increase in $q$ leads to a more rapid convergence of both solutions onto a velocity profile that matches the original solution. Additionally, it is worthwhile to note the "potential flow-like" mean flow for the Type I solution at $q = 2$, which was previously only associated with the Hart-McClure classic profile.[33, 65] Its characteristics mirror those of the Hart-McClure mean flow in the radial and axial directions, which indicate a uniform axial velocity profile and a linearly decreasing radial velocity as $r \to 0$. However, the Trkalian swirl velocity is observed to decrease to an asymptotic result as the distance to the wall is successively increased. These observations are quite similar to those of the Type I class of solutions described in Saad and Majdalani's work, although velocity magnitudes remain different. In the case of the Type II model, similar behavior is observed to that reported for the Taylor-Culick comparative analysis. Once again, indications of "velocity overshoot" in the radial direction is identified, as well along with a seemingly parabolic axial velocity, which is most pronounced at the $q = 2$ case, for which a peak axial velocity ratio

is achieved at the chamber axis where we may calculate $u_z(0,z)/z \approx 31.24$. In the following chapter, these results will be further evaluated as well as discussed in the context of a numerical verification.

# Chapter 6

# Optimization Results and Discussion

This chapter further evaluates the optimized flowfields to assess, at various values of $q$, the velocities and pressures relative to the exact, partial solution of Chapter 3. Additionally, the flowfield results are further validated using numerical and computational fluid dynamics techniques. As this research has been well communicated to the community over the course of its development, the methods presented in the subsections of this chapter have been previously published by the author and his advisor, and with the support of Dr. Tony Saad who has studied these optimization methods on the Taylor-Culick solution[32, 33,59, 60] . One exception is the content regarding the verification methods demonstrated for the energy-optimized solutions, which have not been previously published, although the methodology employed are similar to that of the exact solution presented in Chapter 4[55].

## 6.1 Energy Density Analysis

Consistent with the energy-based optimization performed in Chapter 5, we may evaluate the change in energy content for each solution as $q$ is increased. As shown in Figure 6.1, both Type I and Type II solutions indeed converge upon the original energy density, with variation beyond $q = 7$ becoming negligible. The variation of energy densities at low values of $q$ are interesting: The Type I solution demonstrates a kinetic energy content that is 68% lower than

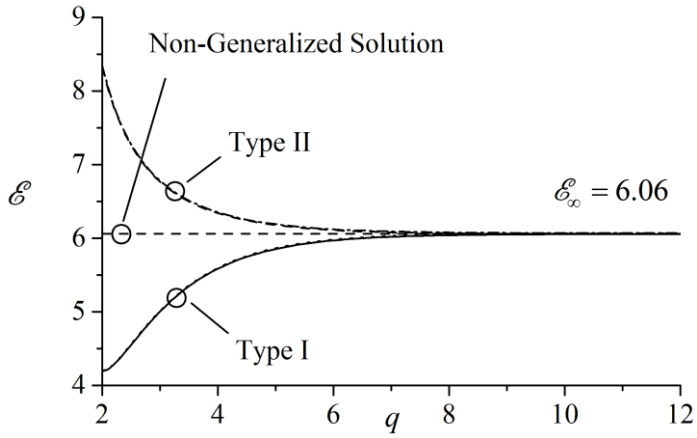


**Figure 6.1 Depiction of energy density approaching an asymptote with increasing $q$.**

that of the base model, while the Type II model reveals to an energy content that is 37.5% higher than the "first root" eigensolution. It is instructive to again note that the lower-energy Type I solutions correspond to the velocity profiles that exhibit "potential-flow-like" behavior and is accompanied by a lower energy content.

## 6.2 Pressure Analysis

The remaining analyses of the optimized solutions focus on geometric configurations with length ratios greater than critical length $L_{cr} \approx 4.415$. This is consistent with the architecture of most solid rocket motor configurations, which typically exceed $L = 20$, and allows the simplified solutions to be used. The pressure field for the flow are described via the methods identified in Saad and Majdalani's discussion of pressure integration.[66] Provided that the two constraints below are satisfied, the pressure field may be described by the total differential:

$$\mathrm{d}p_n = \frac{\partial p_n}{\partial r}\mathrm{d}r + \frac{\partial p_n}{\partial z}\mathrm{d}z \quad \text{or} \quad p_n = \int \frac{\partial p_n}{\partial r} dr + \int \frac{\partial p_n}{\partial z} dz \tag{6.1}$$

$$p_n = \int \left( \frac{u_{\theta,n}^2}{r} - u_{r,n}\frac{\partial u_{r,n}}{\partial r} - u_{z,n}\frac{\partial u_{r,n}}{\partial z} \right)\mathrm{d}r + \int \left( -u_{r,n}\frac{\partial u_{z,n}}{\partial r} - u_{z,n}\frac{\partial u_{z,n}}{\partial z} \right)\mathrm{d}z \tag{6.2}$$

This step enables us to write

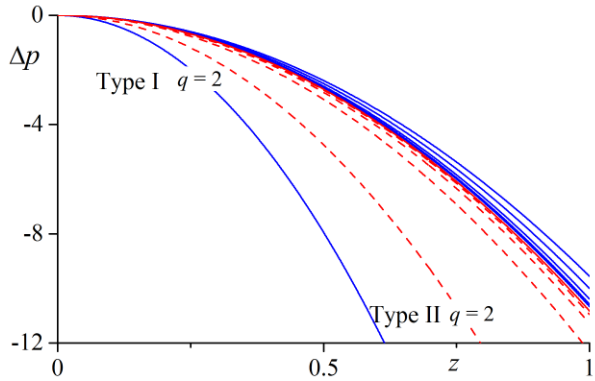


**Figure 6.2 Centerline Pressure Variation with increasing** $q$.

$$p(r,z) = p_0 - \tfrac{1}{2}\sum_{n=1}^{\infty}\alpha_n^2\left\{J_1^2(\lambda_n r) + z^2\lambda_n^2\left[J_0^2(\lambda_n r) + J_1^2(\lambda_n r)\right]\right\} \tag{6.3}$$

where each partial differential equation is derived from Euler's momentum conservation relations given by Eqs. (2.7) and (2.8). Our assumptions remain valid provided that the first constraint is satisfied when

$$\frac{\partial^2 p}{\partial r \partial z} = \frac{\partial^2 p}{\partial z \partial r} = \frac{2z\alpha_n^2\lambda_n^2 J_1^2(\lambda_n r)}{r} \tag{6.4}$$

Because of the constraint being shown is indeed valid, a pressure profile may be produced, namely,

$$\mathrm{d}p_n = \frac{\partial p_n}{\partial r}\mathrm{d}r + \frac{\partial p_n}{\partial z}\mathrm{d}z \tag{6.5}$$

or

$$p_n = \int \frac{\partial p_n}{\partial r}\mathrm{d}r + \int \frac{\partial p_n}{\partial z}\mathrm{d}z \tag{6.6}$$

$$p_n = \int\left(\frac{u_{\theta,n}^2}{r} - u_{r,n}\frac{\partial u_{r,n}}{\partial r} - u_{z,n}\frac{\partial u_{r,n}}{\partial z}\right)\mathrm{d}r + \int\left(-u_{r,n}\frac{\partial u_{z,n}}{\partial r} - u_{z,n}\frac{\partial u_{z,n}}{\partial z}\right)\mathrm{d}z \tag{6.7}$$

$$\Delta p(r,z) = p(r,z) - p_0 = -\tfrac{1}{2}\sum_{n=1}^{\infty}\alpha_n^2\left\{J_1^2(\lambda_n r) + z^2\lambda_n^2\left[J_0^2(\lambda_n r) + J_1^2(\lambda_n r)\right]\right\} \tag{6.8}$$

This pressure profile can be validated by to show that it satisfies the original continuity, Euler momentum, and vorticity transport equations. Following this, the pressure profile is described against varying $q$, as shown in Figure 6.2 for the centerline case.

## 6.3 Numerical Verification of Energy-Steepened Solution

Utilizing the same methodology and construct as presented in Chapter 4 for the exact solution, the energy optimized solutions were developed and studied. The results for an initial wall velocity of 10 m/s are presented in Appendix B, with comparisons made between analytical and numerical solutions for component velocity and pressure, demonstrating general agreement across the flow fields. CFD solutions for both Type I and Type II forms were studied, with $q$ varying from $2 \le q \le 6$, however convergence of the solution was not achieved for the $q = 2$ and $q = 3$ forms, and as a result no comparison is presented. The reason for the lack of convergence may be due to the general "severity" of the velocity profiles observed in their potential flow like behavior, and its incompatibility with the use of the pressure boundary in the far field. These deviations, relative to the solutions at higher values of $q$, may be observed and compared in Figure 5.2.

Nevertheless, in the solutions presented, velocity profiles in each component direction are shown at various axial stations, while centerline pressure profile agreement is also demonstrated. One curious element that was studied but ultimately unresolved was the requirement of a scale factor, which varies with $q$, to be applied to the analytically-predicted pressure drop in order to align with the results generated via CFD. Beyond the application of a scale factor for the solution, the profile shapes of the pressure drop between the analytical and CFD solutions are consistent. Moreover, the scale factor required was not monotonically varying with changing $q$ in the case of the Type I solution, as denoted on each comparison in Appendix B. This peculiar behavior may be linked to an unaccounted element that is linked to the pressure behavior observed for the Type I analytical solution depicted in Figure 6.2. An additional issue that was identified in analysis of the results was that the influence of the far-field pressure boundary does, in some instances, extend further into the field than the initial screening process implied, and as a result, the Type I, $q = 4$ shows some divergence in the swirl velocity component as it approaches

the far field. However, its consistency with the analytical solution further upstream lends credence to the method in general, but implies that a greater length to accommodate the far field should be applied in future work. Overall, the CFD and analytical solutions demonstrated good agreement in all velocity components, thus confirming all of the trends in velocity changes as the energy index changes.

In order to inject additional confidence in the proposed solutions, we may verify that the underlying PDE solution is appropriately constructed. By introducing the transformation $\psi = zF(r)$ to Equation (3.12) may be re-written as a linear ordinary differential equation. Indeed, it may be seen that

$$\frac{\partial^2 \psi}{\partial r^2} - \frac{1}{r}\frac{\partial \psi}{\partial r} + \frac{\partial^2 \psi}{\partial z^2} + \mathcal{C}^2 \psi = 0 \tag{3.12}$$

becomes

$$F''(r) - \frac{1}{r}F'(r) + \lambda_1^{\,2} F(r) = 0 \tag{6.9}$$

with boundary conditions specified via

$$\begin{cases} u_r(0,z) = 0 \Rightarrow F(0) = 0 & \text{(a)} \\ u_r(1,z) = -1 \Rightarrow F(1) = 1 & \text{(b)} \end{cases} \tag{6.10}$$

In order to develop the eigenfunction solutions via numerical evaluation, we must acknowledge each solution's linear independence by solving for the individual eigensolutions and summing them find the total. By setting the following equality

$$F(r) = \sum_{1}^{\infty} F_n(r) \tag{6.11}$$

It then further requires the following ODE for each eigenfunction

$$F_n''(r) - \frac{1}{r}F_n'(r) + \lambda_n^{\,2} F_n(r) = 0 \tag{6.12}$$

with boundary conditions transformed to become

$$\begin{cases} F_n(0) = 0 \quad \Rightarrow \; F(0) = \sum F_n(0) = 0 & \text{(a)} \\ F_n(1) = J_1(\lambda_n)\alpha_n \Rightarrow \; F(1) = \sum F_n(1) = \sum J_1(\lambda_n)\alpha_n = 1 & \text{(b)} \end{cases}; \tag{6.13}$$

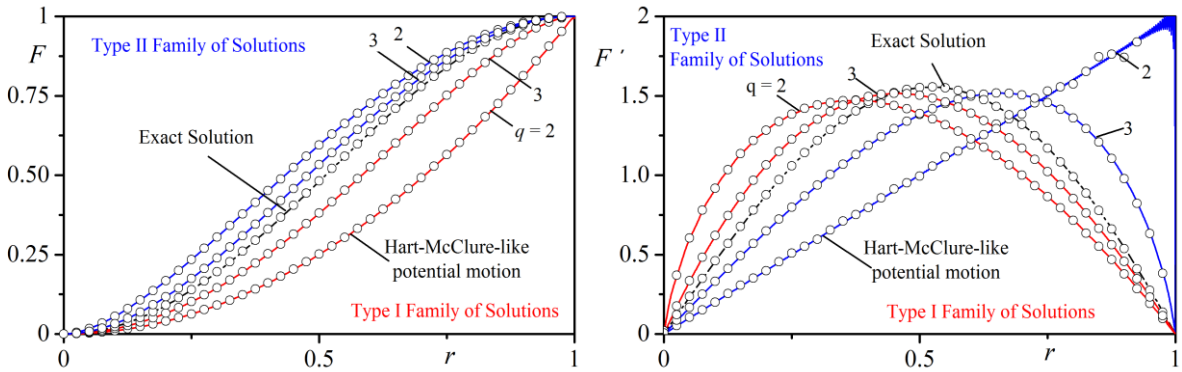


**Figure 6.3 Verifying depiction of numerical (circles) and analytical solutions for transformed stream function equation $F(r) = \psi / z$ and its derivative.**

Eqs. (6.12) and (6.13) may then be solved for different values of the energy index $q$ using Mathematica's *NDSolve* utility. Because we possess boundary values in this problem, the NDSolve utility is configured to use the "shooting" method. Results of the numerical integration are shown in Figure 6.3, where values of F and F' are compared between the numerical results (filled circles) and the analytical streamfunction solutions (lines) described in Figure 6.3. It is readily evident that both Type I and Type II numerical solutions well-match their analytical counterparts at various values of $q$. The numerical procedure was capable of reproducing the solutions presented in this work, and visual differences between the numerical and analytical solutions are hardly distinguishable, with the small exception of the development of minor instability in the computed analytical solution for the "potential-flow-like" field of the Type I, $q = 2$ solution.

# Chapter 7

# Conclusion

## 7.1 Significant Contributions

In contemplating the value of the work to the current body of knowledge, it is worthwhile to succinctly recap the work that was presented:

- A primer described the available body of knowledge regarding the application and refinement of the classic Taylor-Culick flowfield
- The development of the TC flowfield was explored, with discussion provided about specific relations that are implied and indeed required to develop the classic field, but that inhibit the swirling flow that has been identified in experiments and would likely be present in spin-stabilized rocket motors
- An new solution is constructed using alternative relations that does allow a swirl component to develop
- The new solution was demonstrated to have multiple forms that satisfy the underlying differential equation, which may be cataloged by total kinetic energy content
- The solutions were validated utilizing numerical verification and computational fluid dynamics techniques.

It is hoped that the level of detail provided in this work, both in the formulation the solution and the execution of its analysis, will be valuable to the academic community in the pursuit of further research.

## 7.2 Future Work

As identified in Chapter 1, a number of opportunities for future refinement and application may exist for the flowfields presented. Regarding refinement, some work is already underway, with Majdalani making substantive contributions to the field in the form of viscous effects accounting[49] and Cecil and Majdalani addressing compressibility effects and arbitrary headwall injection[67]. Additionally, the previous work of Majdalani and associates point to a number of other relevant studies that may be considered, to include stability analysis[10], particle-flow interactions[10] and wave propagation & mode coupling methods[68, 69], while the work of others offer opportunity in the realms of reactive flows[18, 19, 70] and the field's applicability to hybrid rocket motors[15-17]. Indeed, much of the body of effort revolving around the Taylor-Culick solution may be reviewed to determine if additional merit exists in applying the new flowfield to those topics. The author also has an interest in enhancing the work with a look to other optimization parameters, to include specific swirl content optimization vs the total energy methods presented in this work, as well as performing some first-pass applications of the field to the acoustics concepts that are of high interest to the rocketry community. Overall, It is hoped that the fields presented in this work and published works are found to be well-founded and relevant to future studies of solid rocket motors and other relevant systems.

## 7.3 Lessons Learned

As is natural in any academic research, a number of lessons were learned over its course that, in the absence of constraints on time and resources, would be used to revise various components. As it is hoped that this work might be carried on by other researchers, the following items were identified that may prove valuable to others seeking to further the work:

- In the validation of the energy-optimized solutions, I would have utilized a longer aspect ratio tube relative to the area of interest. The reasons for this are two-fold – the

application of the pressure boundary as an outlet produces distorted fields near its boundary, which drove me to set aside the last 20% of the tube length to accommodate those effects. It was later recognized that some of the converged solutions (specifically the Type I, Q=4) solution were still impacted by the presence of be boundary at that arbitrary demarcation. Secondly, increasing the aspect ratio would have provided more opportunity to graphically see the effects of the energy optimized flows in the CFD and line plots – as it stands it is apparent that while all of the trends are verified through the CFD analysis, it requires a careful eye to appreciate the variation between the various energy indexes. In retrospect, doubling the length to an aspect ratio of 20 with additional room reserved for demarking the boundary-affected area would have been beneficial. Unfortunately, the use a longer tube at the time the issue was identified would have required a complete re-write of the CFD mesh, initialization files, solutions, and associated analytical comparisons.

- A curious result was identified in the CFD analysis that went investigated but ultimately was not fully resolved, specifically regarding the comparison of pressure between the analytical and CFD solutions of the energy-optimized solution. For each value of $q$, a single, constant scale factor that varied non-monotonically across values of $q$ was applied to the analytical prediction in order to align the two results. The correction scaling factors ranged between 0.8933 and 1.06, and were applied to the analytical predictions. The variation and non-monotonic nature of the variation with q may simply be a latent effect of the CFD pressure boundary having unanticipated and inconsistent effects beyond the velocity effects otherwise clearly observed in the last 20% of the overall solution space. Beyond the scale factor, the analytical prediction and CFD result otherwise maintained a similar and appropriate shape, as evidenced by the comparisons shown in Appendix B, wherein the utilized scale factors are noted. This topic deserves additional study, however confidence is generally maintained in the methods because the both the exact, non-optimized solution reported no appreciable difference, and several of the energy optimized solutions achieved consistency within ~1%.

## 7.4 Personal Development

Overall, this research has proved to be an excellent opportunity to conduct an independent investigation. The effort incorporated a number of valuable skill development opportunities, useful in both academic and industry effort in the future. The application of engineering concepts refined in coursework - to include Differential Equations, Variational Calculus, Aerodynamics, and Fluid Mechanics - were critical to the development and interpretation of the new solutions. Additionally, numerous skills were further developed that will be beneficial throughout an engineering career. Literature research and interviews with my advisor and other peers that have executed similar effort proved invaluable to understanding the state of the research, and provided useful guidance on how to proceed. The development of solutions from first principles, the use of optimization & numerical verification techniques, and skill building in computational fluid dynamics were all very relevant exercises that many engineers would find useful when applying their knowledge and experience to engineering challenges. Furthermore, this work has provided ample opportunity to develop skill in academic communication, with opportunity to contribute both to conference proceedings and academic journals.

It has been a true honor to make this small contribution to the academic community, and I hope that it serves to be both informative and foundational to future work.

# References

1. Culick, F.E.C., *Rotational axisymmetric mean flow and damping of acoustic waves in a solid propellant rocket.* AIAA Journal, 1966. **4**(8): p. 1462-1464.

2. Griffond, J., G. Casalis, and J. Pineau, *Spatial instability of flow in a semiinfinite cylinder with fluid injection through its porous walls.* European Journal of Mechanics B/Fluids, 2000. **19**(1): p. 69-87.

3. Majdalani, J., G. Flandro, and T. Roh, *Convergence of two flowfield models predicting a destabilizing agent in rocket combustion.* Journal of Propulsion and Power, 2000. **16**(3): p. 492-497.

4. Chedevergne, F., G. Casalis, and T. Féraille, *Biglobal linear stability analysis of the flow induced by wall injection.* Physics of Fluids, 2006. **18**(1): p. 014103-14.

5. Abu-Irshaid, E.M., J. Majdalani, and G. Casalis, *Hydrodynamic stability of rockets with headwall injection.* Physics of Fluids, 2007. **19**(2): p. 024101-11.

6. Chedevergne, F., G. Casalis, and J. Majdalani, *Direct numerical simulation and biglobal stability investigations of the gaseous motion in solid rocket motors.* Journal of Fluid Mechanics, 2012. **706**: p. 190-218.

7. Ugurtas, B., et al., *Stability and acoustic resonance of internal flows generated by side injection*, in *Solid Propellant Chemistry, Combustion, and Motor Interior Ballistics*, V. Yang, T.B. Brill, and W.-Z. Ren, Editors. 2000, AIAA Progress in Astronautics and Aeronautics: Washington, DC. p. 823-836.

8. Fabignon, Y., et al., *Instabilities and pressure oscillations in solid rocket motors.* Journal of Aerospace Science and Technology, 2003. **7**(3): p. 191-200.

9. Féraille, T. and G. Casalis, *Channel flow induced by wall injection of fluid and particles.* Physics of Fluids, 2003. **15**(2): p. 348-360.

10. Bhatia, L., et al. *Stability of the Taylor-Culick profile with headwall injection and particle interactions*. in *AIAA*. 2006. Sacramento, CA.

11. Féraille, T., G. Casalis, and J. Dupays. *Particle effects on solid-propellant motors flow stability*. in *AIAA*. 2002.

12. Griffond, J. and G. Casalis, *On the nonparallel stability of the injection induced two-dimensional Taylor flow.* Physics of Fluids, 2001. **13**(6): p. 1635-1644.

13. Beddini, R.A. and T.A. Roberts, *Turbularization of an acoustic boundary layer on a transpiring surface.* AIAA Journal, 1988. **26**(8): p. 917-923.

14. Griffond, J., *Receptivity and aeroacoustic resonance in channels with blowing walls.* Physics of Fluids, 2002. **14**(11): p. 3946-3962.

15. Najjar, F., et al., *Simulations of solid-propellant rockets: Effects of aluminum droplet size distribution.* Journal of Spacecraft and Rockets, 2006. **43**(6): p. 1258-1270.

16. Balachandar, S., J.D. Buckmaster, and M. Short, *The generation of axial vorticity in solid-propellant rocket-motor flows.* Journal of Fluid Mechanics, 2001. **429**(1): p. 283-305.

17. Haselbacher, A., et al., *Slow-time acceleration for modeling multiple-time-scale problems.* Journal of Computational Physics, 2010. **229**(2): p. 325-342.

18. Chu, W., V. Yang, and J. Majdalani, *Premixed flame response to acoustic waves in a porous-walled chamber with surface mass injection.* Combustion and Flame, 2003. **133**(3): p. 359-370.

19. Kim, J., P. Moin, and R. Moser, *Turbulence statistics in fully developed channel flow at low Reynolds number*. J. fluid mech., 1987. **177**: p. 133.

20. Majdalani, J. and M. Akiki, *Rotational and quasiviscous cold flow models for axisymmetric hybrid propellant chambers.* Journal of Fluids Engineering, 2010. **132**(10): p. 101202-7.

21. Xu, H., et al., *Homotopy based solutions of the Navier-Stokes equations for a porous channel with orthogonally moving walls.* Physics of Fluids, 2010. **22**(5): p. 05360101-18.

22. Xu, H., et al., *Homotopy based solutions of the Navier-Stokes equations for a porous channel with orthogonally moving walls.* Physics of Fluids, 2010. **22**(5): p. 05360101-18.

23. Majdalani, J., A. Vyas, and G. Flandro, *Erratum on higher mean-flow approximation for a solid rocket motor with radially regressing walls.* AIAA Journal, 2009. **47**(1): p. 286-286.

24. Kurdyumov, V.N., *Steady flows in the slender, noncircular, combustion chambers of solid propellants rockets.* AIAA Journal, 2006. **44**(12): p. 2979-2986.

25. Majdalani, J., *On steady rotational high speed flows: the compressible Taylor-Culick profile.* Proceedings of the Royal Society of London, Series A, 2007. **463**(2077): p. 131-162.

26. Maicke, B.A. and J. Majdalani, *On the rotational compressible Taylor flow in injection-driven porous chambers.* Journal of Fluid Mechanics, 2008. **603**(1): p. 391-411.

27. Majdalani, J. and T. Saad, *The Taylor-Culick profile with arbitrary headwall injection.* Physics of Fluids, 2007. **19**(9): p. 093601-10.

28. Traineau, J.C., P. Hervat, and P. Kuentzmann. *Cold-flow simulation of a two-dimensional nozzleless solid-rocket motor*. in *AIAA*. 1986. Huntsville, AL.

29. Balakrishnan, G., A. Liñan, and F.A. Williams, *Rotational inviscid flow in laterally burning solid propellant rocket motors.* Journal of Propulsion and Power, 1992. **8**(6): p. 1167-1176.

30. Akiki, M. and J. Majdalani. *Exact solutions for the integral form of the compressible flowfield in a porous cylinder*. in *AIAA*. 2011. San Diego, CA.

31. Akiki, M. and J. Majdalani, *Improved integral form of the compressible flowfield in thin channels with injection.* AIAA Journal, 2012. **50**(2): p. 485-493.

32. Majdalani, J. and T. Saad, *Internal Flows Driven by Wall-Normal Injection*, in *Advanced Fluid Dynamics*, H.W. Oh, Editor. 2012, InTech: Rijeka, Croatia. p. 95-134.

33. Saad, T. and J. Majdalani, *On the Lagrangian optimization of wall-injected flows: from the Hart–McClure potential to the Taylor–Culick rotational motion.* Proceedings of the Royal Society of London, Series A, 2010. **466**(2114): p. 331-362.

34. Taylor, G., *Fluid flow in regions bounded by porous surfaces.* Proceedings of the Royal Society of London, Series A, 1956. **234**(1199): p. 456-475.

35. Dunlap, R., P. Willoughby, and R. Hermsen, *Flowfield in the combustion chamber of a solid propellant rocket motor.* AIAA Journal, 1974. **12**(10): p. 1440-1445.

36. Baum, J.D., J.N. Levine, and R.L. Lovine, *Pulsed instabilities in rocket motors: A comparison between predictions and experiments.* Journal of Propulsion and Power, 1988. **4**(4): p. 308-316.

37. Sabnis, J., H. Gibeling, and H. McDonald, *Navier-Stokes analysis of solid propellant rocket motor internal flows.* Journal of Propulsion and Power, 1989. **5**(6): p. 657-664.

38. Apte, S.V. and V. Yang, *Effect of acoustic oscillation on flow development in a simulated nozzleless rocket motor*, in *Solid Propellant Chemistry, Combustion, and Motor Interior Ballistics*, V. Yang, T.B. Brill, and W.Z. Ren, Editors. 2000, AIAA Progress in Astronautics and Aeronautics: Washington, DC. p. 791-822.

39. Yamada, K., M. Goto, and N. Ishikawa, *Simulative study on the erosive burning of solid rocket motors.* AIAA Journal, 1976. **14**(9): p. 1170-1176.

40. Dunlap, R., et al., *Internal flow field studies in a simulated cylindrical port rocket chamber*. Journal of Propulsion and Power, 1990. **6**(6): p. 690-704.

41. Avalon, G. and D. Lambert, *Campagne d'essais VALDO, période 2000/2001*. 2001, ONERA, Establissement de Palaiseau.

42. Casalis, G., G. Avalon, and J.-P. Pineau, *Spatial instability of planar channel flow with fluid injection through porous walls.* Physics of Fluids, 1998. **10**(10): p. 2558-2568.

43. Majdalani, J. and T. Roh, *The oscillatory channel flow with large wall injection.* Proceedings of the Royal Society of London, Series A, 2000. **456**(1999): p. 1625-1657.

44. Clayton, C.D. *Flowfields in solid rocket motors with tapered bores*. in *AIAA*. 1996.

45. Barron, J., J. Majdalani, and W.K. Van Moorhem, *A novel investigation of the oscillatory field over a transpiring surface.* Journal of Sound and Vibration, 2000. **235**(2): p. 281-297.

46. Majdalani, J. and W.K. Van Moorhem, *Laminar cold-flow model for the internal gas dynamics of a slab rocket motor.* Journal of Aerospace Science and Technology, 2001. **5**(3): p. 193-207.

47. Zhou, C. and J. Majdalani, *Improved mean-flow solution for slab rocket motors with regressing walls.* Journal of Propulsion and Power, 2002. **18**(3): p. 703-711.

48. Kuentzmann, P., *Combustion Instabilities*. AGARD LS 180. Vol. September. 1991: AGARDograph.

49. Majdalani, J. and A. Fist. *Improved Mean Flow Solution for Solid Rocket Motors with a Naturally Developing Swirling Motion*. in *50th AIAA Joint Propulsion Conference*. 2014. Cleveland, Ohio.

50. Fist, A. and J. Majdalani. *Improved Mean Flow Solution for Solid Rocket Motors*. in *52nd Aerospace Sciences Meeting*. 2014. National Harbor, MD.

51. Fist, A., J. Majdalani, and T. Saad. *Energy Steepened States of the Swirling Mean Flow in a Solid Rocket Motor*. in *50th AIAA Joint Propulsion Conference*. 2014. Cleveland, Ohio.

52. Batchelor, G.K., *An Introduction to Fluid Dynamics*. 1967, Cambridge: Cambridge University Press.

53. Vyas, A. and J. Majdalani, *Exact solution of the bidirectional vortex.* AIAA Journal, 2006. **44**(10): p. 2208-2216.

54. Majdalani, J., *Helical solutions of the bidirectional vortex in a cylindrical cyclone: Beltramian and Trkalian motions.* Fluid Dynamics Research, 2012. **44**(6): p. 065506-38.

55. Majdalani, J. and A. Fist, *On the spinning Trkalian mean flow field in solid rocket motors.* Journal of Fluid Mechanics, Submitted 27 Sep 2016; Under Review.

56. Hart, R. and F. McClure, *Combustion instability: acoustic interaction with a burning propellant surface.* The Journal of Chemical Physics, 1959. **30**(6): p. 1501-1514.

57. Culick, F., *Rotational axisymmetric mean flow and damping of acoustic waves in a solid propellant rocket.* AIAA Journal, 1966. **4**(8): p. 1462-1464.

58. McClure, F., R. Hart, and R. Cantrell, *Interaction between sound and flow: stability of T-burners.* AIAA Journal, 1963. **1**(3): p. 586-590.

59. Majdalani, J. and T. Saad. *Energy steepened states of the Taylor-Culick profile*. in *AIAA*. 2007. Cincinnati, OH.

60. Saad, T. and J. Majdalani. *Energy based mean flow solutions for slab hybrid rocket chambers*. in *AIAA*. 2008. Hartford, CT.

61. Saad, T. and J. Majdalani. *Energy based solutions of the bidirectional vortex with multiple mantles*. in *AIAA*. 2009. Denver, CO.

62. Saad, T. and J. Majdalani. *Energy based solutions of the bidirectional vortex*. in *AIAA*. 2008. Hartford, CT.

63. Sneddon, I.N., *On some infinite series involving the zeros of Bessel functions of the first kind.* Proceedings of the Glasgow Mathematical Association, 1960. **4**(03): p. 144-156.

64. Sutton, G.P. and O. Biblarz, *Rocket Propulsion Elements*. 7th ed. 2001, New York: John Wiley.

65. Maicke, B.A., T. Saad, and J. Majdalani, *On the compressible Hart-McClure and Sellars mean flow motions.* Physics of Fluids, 2012. **24**(9): p. 096101-20.

66. Saad, T. and J. Majdalani, *Some thoughts on the pressure integration requirements for the Navier-Stokes equations.* Fluid Dynamics Research, 2012. **44**(7): p. 065508-11.

67. Cecil, O. and J. Majdalani. *On Steady Trkalian High Speed Flows: Swirling Compressible Motions in Rockets with Headwall Injection*. in *51st AIAA/SAE/ASEE Joint Propulsion Conference*. 2015. Orlando, Florida.

68. Majdalani, J. *Asymptotic methods for solving wave propagation problems in porous tubes, channels and spheres*. in *AIAA*. 2010. Chicago, Illinois.

69. Jankowski, T. and J. Majdalani, *Vortical and acoustical mode coupling inside a porous tube with uniform wall suction.* Journal of the Acoustical Society of America, 2005. **117**(6): p. 3448-3458.

70. Chu, W.-W., *Dynamic Responses of Combustion to Acoustic Waves in Porous Chambers with Transpiration*, in *Department of Mechanical Engineering*. 1999, The Pennsylvania State University: College Park.

# Appendices

# Appendix A – CFD Method Details

## Solution Method for Trkalian Profile CFD

Geometry Information

1m Length  x 1m Radius Cylindrical Slice (Box)

Mesh Information

384360 Cells Structured Uniform

113104 Point Profile Points for Initialization Profile

Launcher

Checked Boxes:

- Display Mesh After Reading (Optional)
- Workbench Color Screen
- Double Precision
- Processing Options
    - Parallel (Local Machine)
        - Processes (PC-Dependent… I used 7)

GPGPUs per Machine (PC-Dependent… I used None)

General Setup

- Solver: Pressure-Based
- Time: Steady
- 2D Space Axisymmetric Swirl
- Velocity Formation: Absolute
- Gravity: Unchecked
- Models: All “Off” except Viscous – Inviscid
- Materials: Default (Fluid – Air, Solid – Aluminum)
- Cell Zone Conditions:

1. Click “Profiles…”-> “Read….” -> (Select File with Initial Profile) -> Select Profile in Profile List -> Select Interpolation Method – Least Squares - > Select “Apply”, then Close
2. Select Zone – surface_body -> Select “Edit…” -> Check “Fixed Values” -> Select for each cardinal direction the corresponding velocity name from the profile file (in my case “trak-prof [Axi, rad, swr]” -> Select OK

- Boundary Conditions: Repeat Step 2 of “Cell Zone Conditions” for [headwall] and [sidewall] boundaries
- Dynamic Mesh: Unchecked
- Reference Values: Default values

<u>Solution</u>

Solution Methods:

- Scheme: SIMPLE
- Gradient: Green-Gauss Node Based
- Pressure: PRESTO!
- Momentum: Third-Order MUSCL
- Swirl Velocity: Thrid-Order MUSCL

Solution Controls:

- Pressure: 0.3
- Density: 1
- Body Forces: 1
- Momentum: 0.3
- Swirl Velocity: 0.3
- Equations… : “Flow” and “Swirl Velocity” checked
- Limits: Default
- Advanced: (Not modified)

Monitors: (Not modified)

Solution Initialization:

- Initialization Methods: Hybrid Initialization
- More Settings…:
    - Number of Iterations 15
    - Scalar Equation-0: 1
    - Scalar Equation-1: 1
    - Reference Frame: Relative to Cell Zone
    - Initialization Options: (All unchecked)
- Click "Initialize" (Progress can be viewed in the "Console" Tab)

<u>Solution Process</u>

1. Select – Run Calculation Set:
    - Number of Iterations: 2
    - Reporting Interval: 1
    - Update Interval: 1
2. Select – Data File Quantities:
    - Select Additional Quantities:
        - Static Pressure
        - Total Pressure
        - Velocity Magnitude
        - Axial Velocity
        - Radial Velocity
        - Swirl Velocity
        - Stream Function
3. Select – Calculate
    - Solution should converge on Iteration 1 because the Cell Zone velocities are set to "Fixed Values" … this will interpolate your initial velocity profile and produce an initial solution file
4. Return to Cell Zone Conditions in the Tree and uncheck "Fixed Values" for surface body

5. Return to Run Calculation, set Number of Iterations to [large number, I used 2500], and Calculate, Then when warning appears select "Use settings changes for current and future calculations" and click "OK" … should produce a converged result for my files in about 700 iterations

<u>Results Process</u>

- Quick Check of Profile Contours in each "Data File Quantity" from above:
    - Checked Options:
        - Filled
        - Node Values
        - Global Range
        - Auto Range
    - Levels: 20
    - Setup: 1
    - Graphics –> Contours –> Set Up…
        - Contours of -> Velocity ->
            - [Axial, Radial, Swirl] Velocity
            - [Total, Static] Pressure
            - Stream Function
        - Surfaces -> interior-surface_body
    - Select Display -> Results available on "Graphics" tab

- Extract Data for External Plotting (Excel, Origin)
    1. Create Lines (or Rakes)
        - Select Results from Tree -> Plots -> XY Plot
        - Select New Surface -> Line/Rake…
        - Type [Line or Rake]

- “Line” will contain all points available in a specified path across solution space, while “Rake” allows a specified quantity of equally numbered points across specified path

- Specify End Points
  - For Radial Profiles at [Z=5.0 m]:
    - x0: 5
    - x1: 5
    - y0: 0
    - y1: 1
  - For Axial profiles at [R=0.5]:
    - X0: 0
    - X1: 10
    - Y0: 0.5
    - Y1: 0.5
  - Name each Line a unique name that indicates position
    - Rad-prof[0,2,4,6,8]
    - Axi-prof[point0,point1,point25, point5, point75,1]

2. Select File -> Export -> Solution Data
   - File Type: ASCII
   - Select All Lines/Rakes of Interest
   - Select All Quantities of Interest
     - Axial Velocity
     - Radial Velocity
     - Swirl Velocity
     - Total Pressure
     - Static Pressure

   Select “Write…” - > Save File (File will be ASCII File readable by Notepad or Notepad++, well-behaved for import in to Excel and Origin )

## Appendix B – Detailed CFD Results

The following figures accomplish two objectives – to compare the results of the analytical solutions to those of the CFD solutions, as well as to communicate the continuous contours of several parameters for each CFD solution evaluated. Note that in the case of Figures B.7 – B.13, four additional CFD solutions beyond those with demonstrated results were attempted, but ultimately did not achieve convergence. As a result, and to annotate the work that was attempted, those solutions are listed but marked as "Did Not Converge".

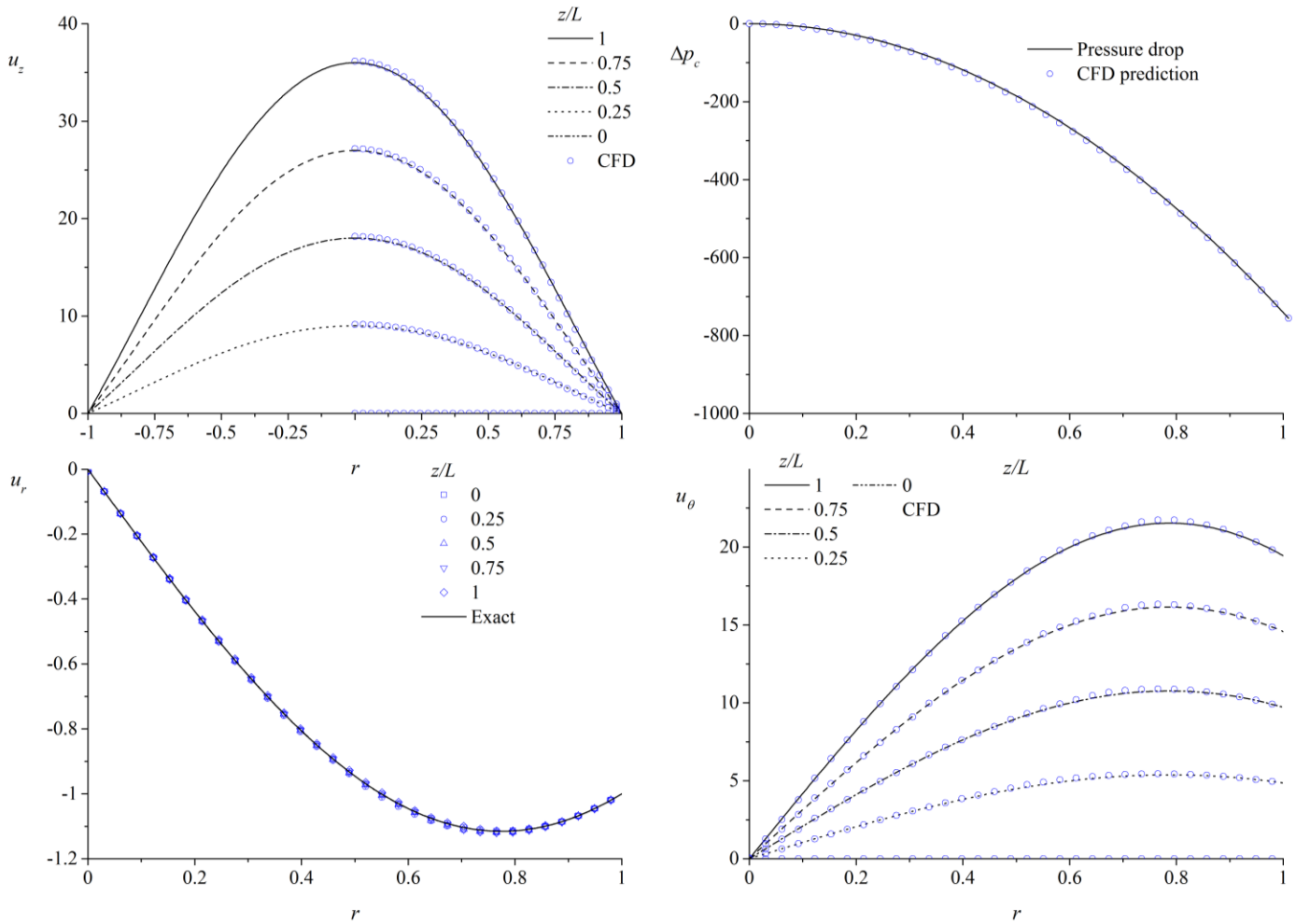


**Figure B.1 Comparison of CFD (circles) and analytical results (lines) Case: Type I, Q=6; Pressure Scale Factor: 0.8933**

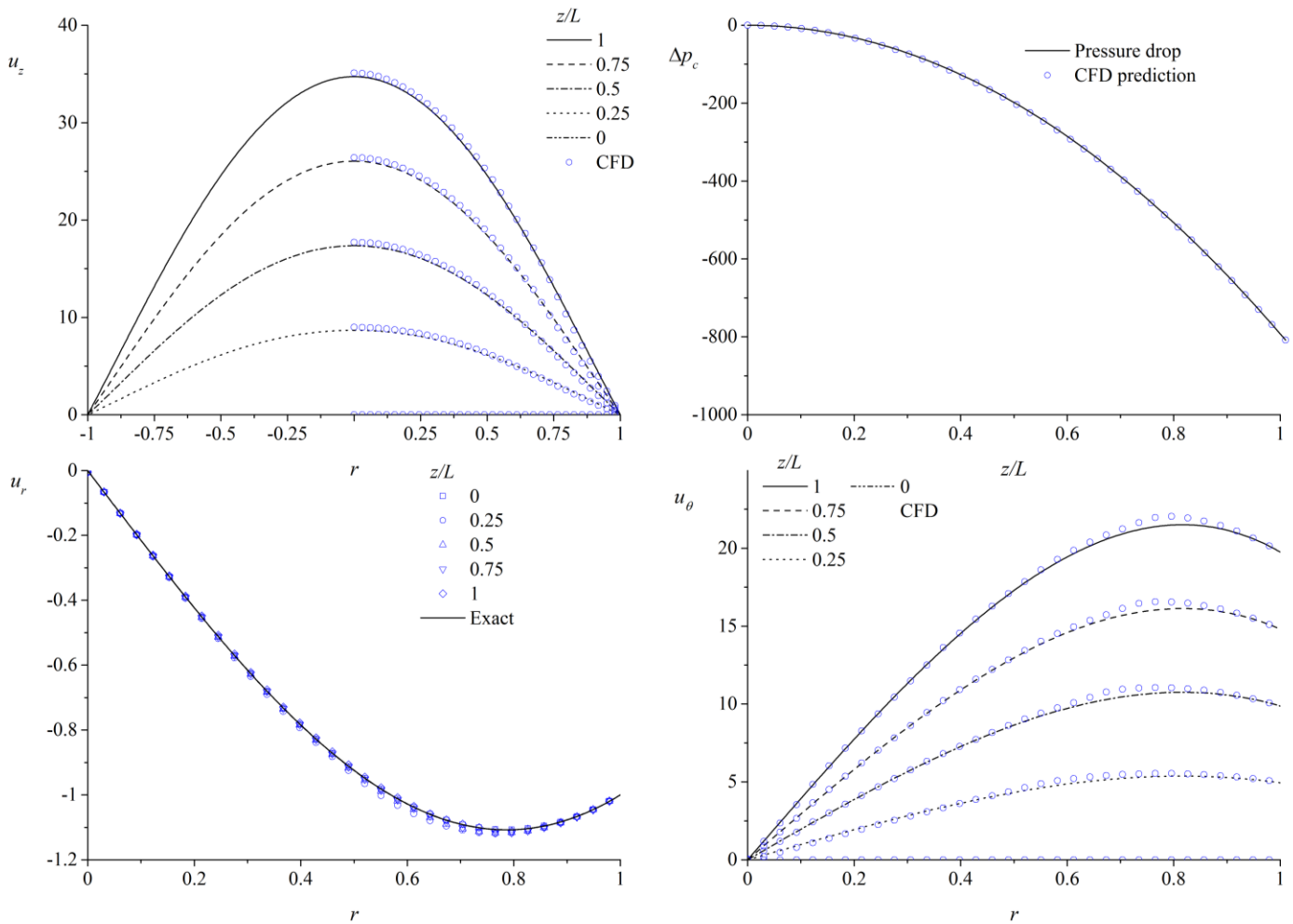


**Figure B.2 Comparison of CFD (circles) and analytical results (lines) Case: Type I, Q=5; Pressure Scale Factor: 0.9726**

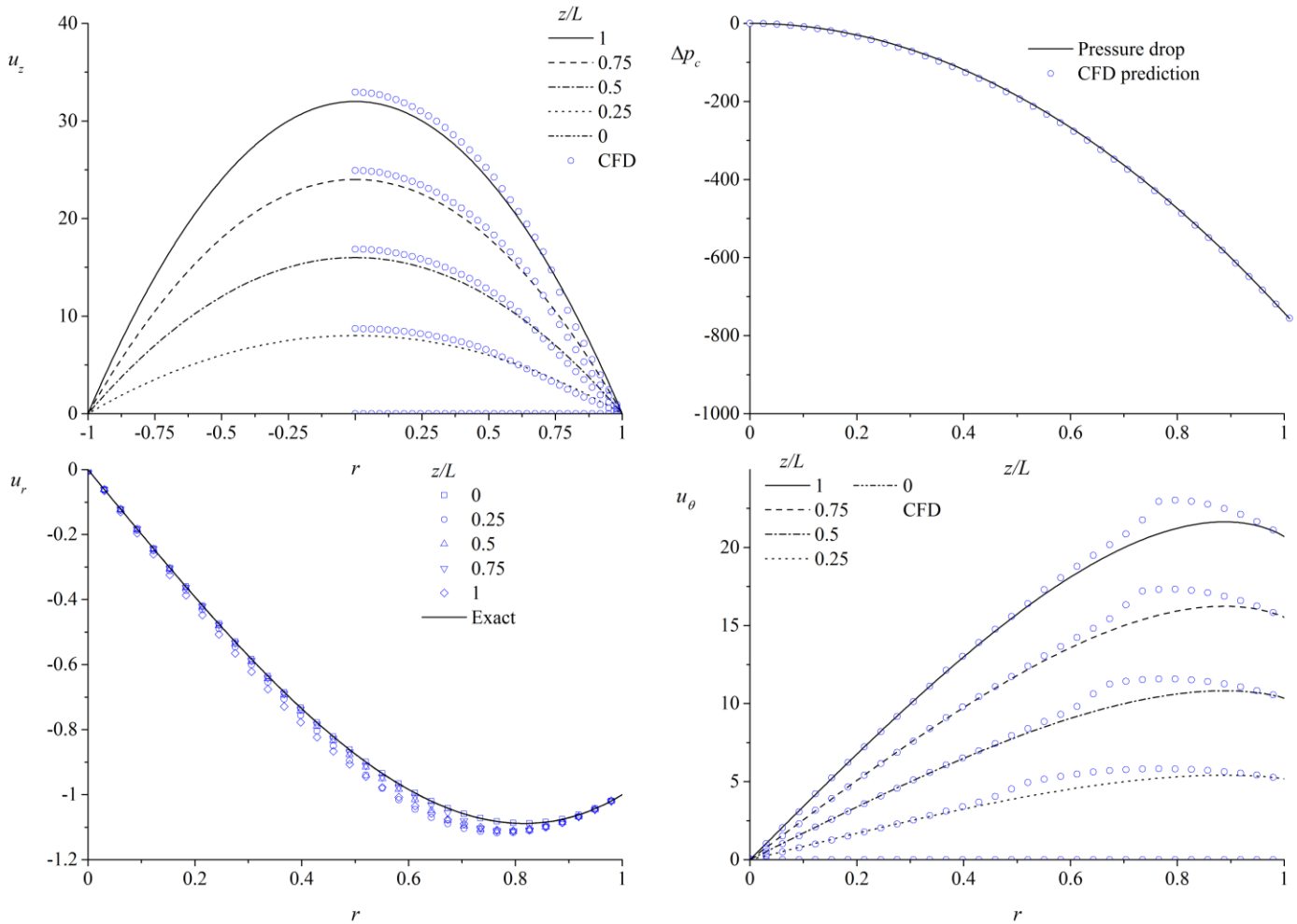


**Figure B.3 Comparison of CFD (circles) and analytical results (lines) Case: Type I, Q=4; Pressure Scale Factor: 0.9455**

Observe that this result demonstrates the effect of the pressure boundary in the far field affecting swirl velocity.

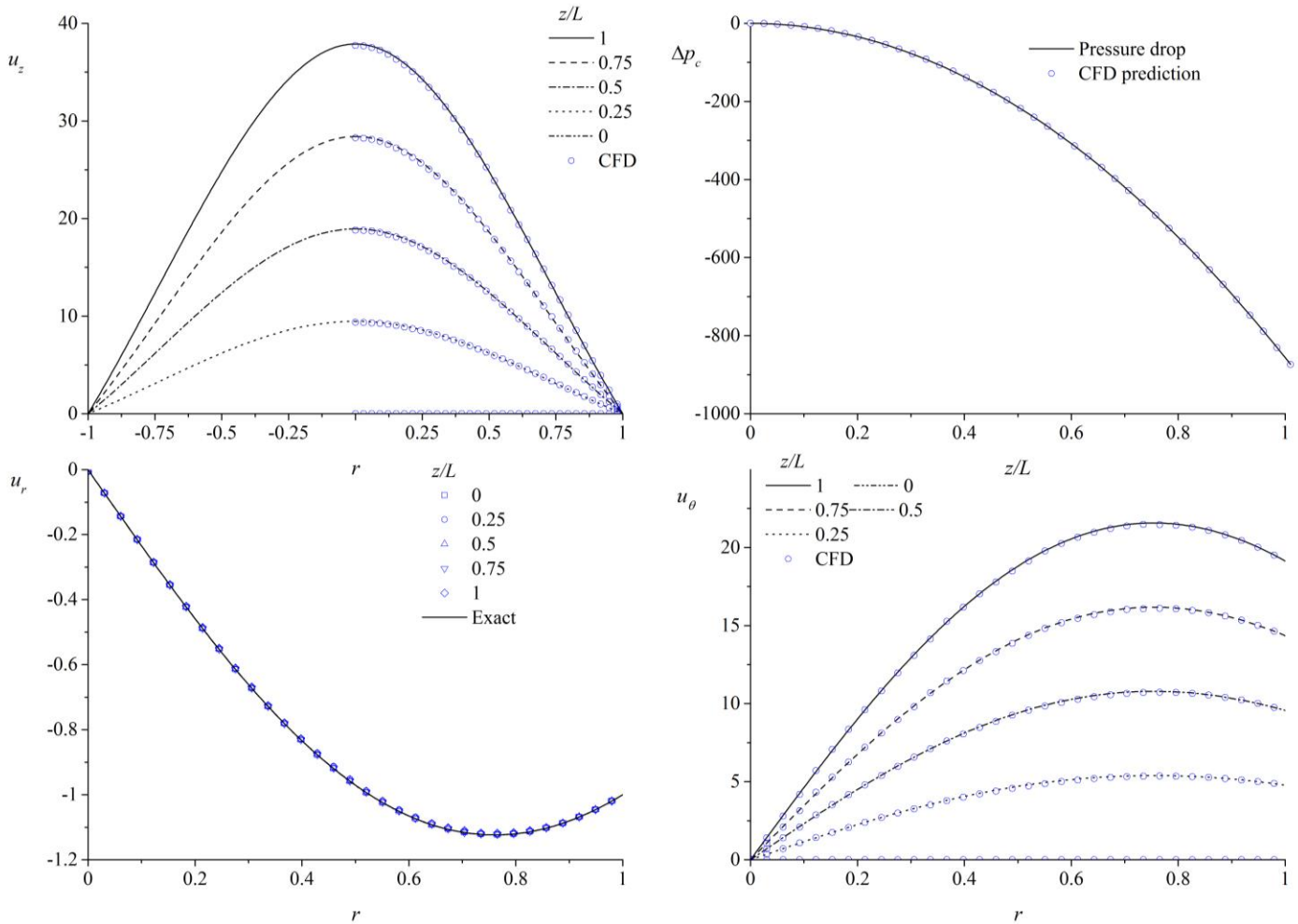


**Figure B.4 Comparison of CFD (circles) and analytical results (lines) Case: Type II, Q=6; Pressure Scale Factor: 1.0102**

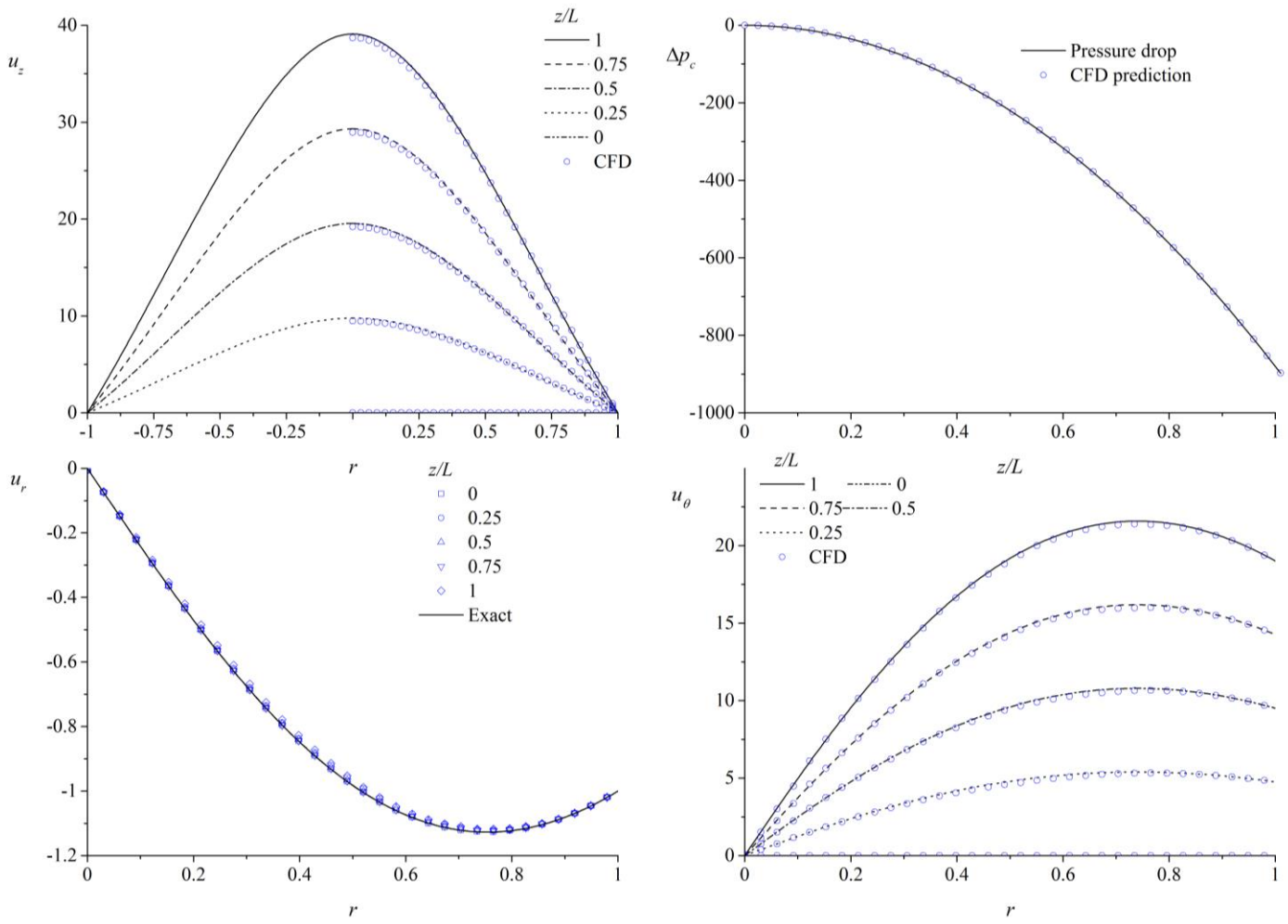


**Figure B.5 Comparison of CFD (circles) and analytical results (lines) Case: Type II, Q=5; Pressure Scale Factor: .9996**

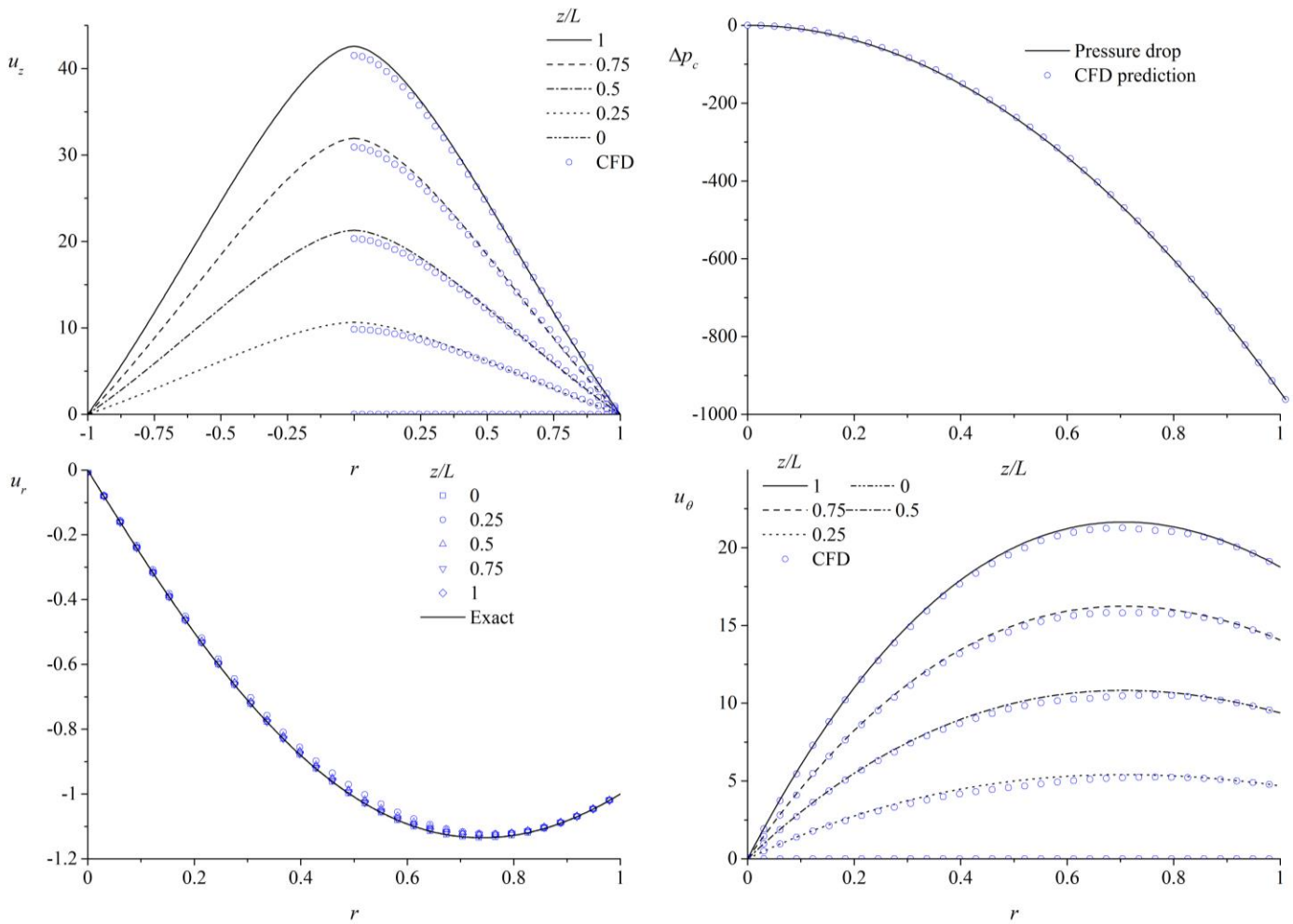


**Figure B.6 Comparison of CFD (circles) and analytical results (lines) Case: Type II, Q=4; Pressure Scale Factor: 1.066**

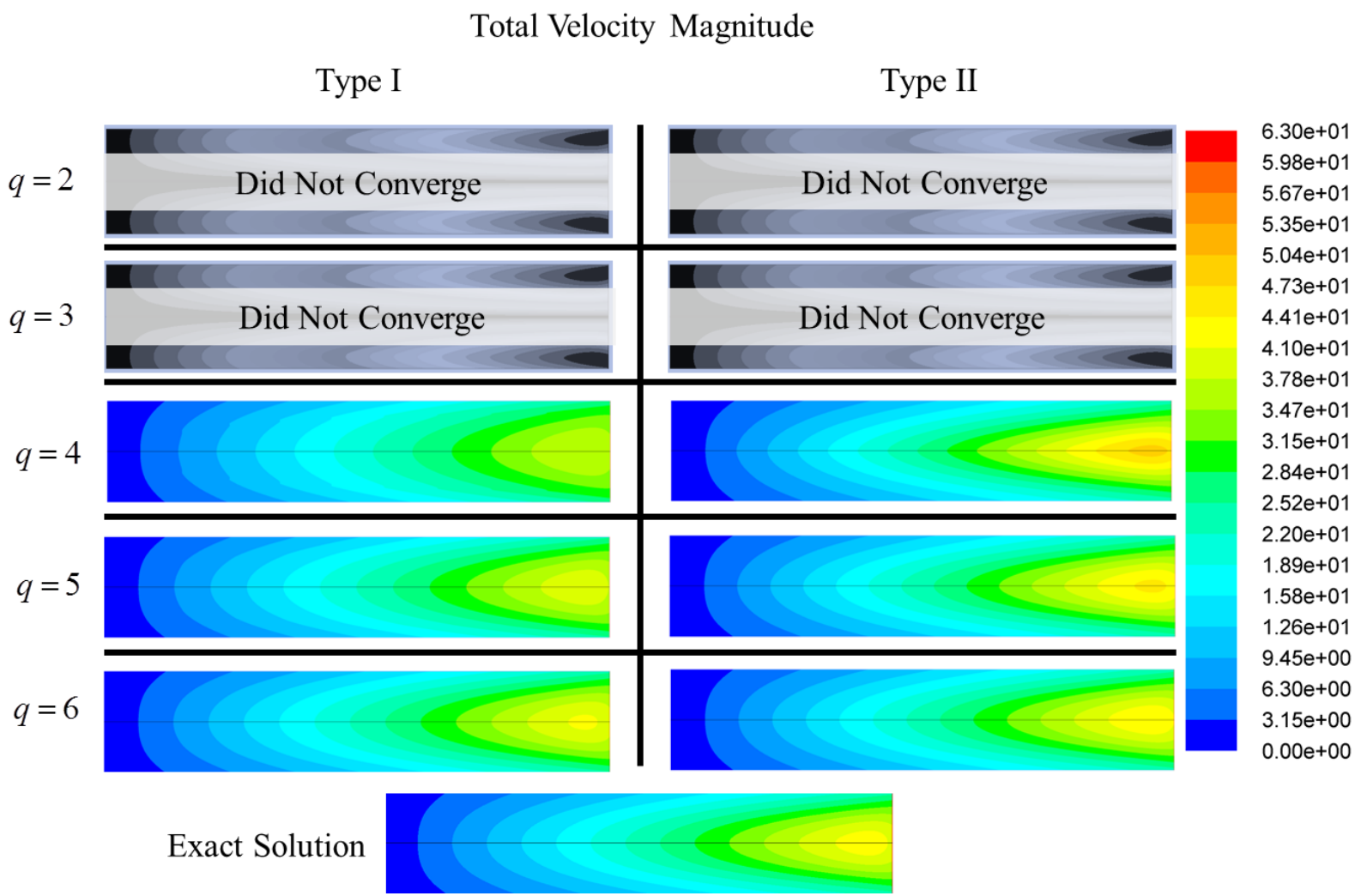


**Figure B.7 Comparison of Contours for Energy-Optimized Type I, Type II and Exact Solutions - Total Velocity Magnitude**

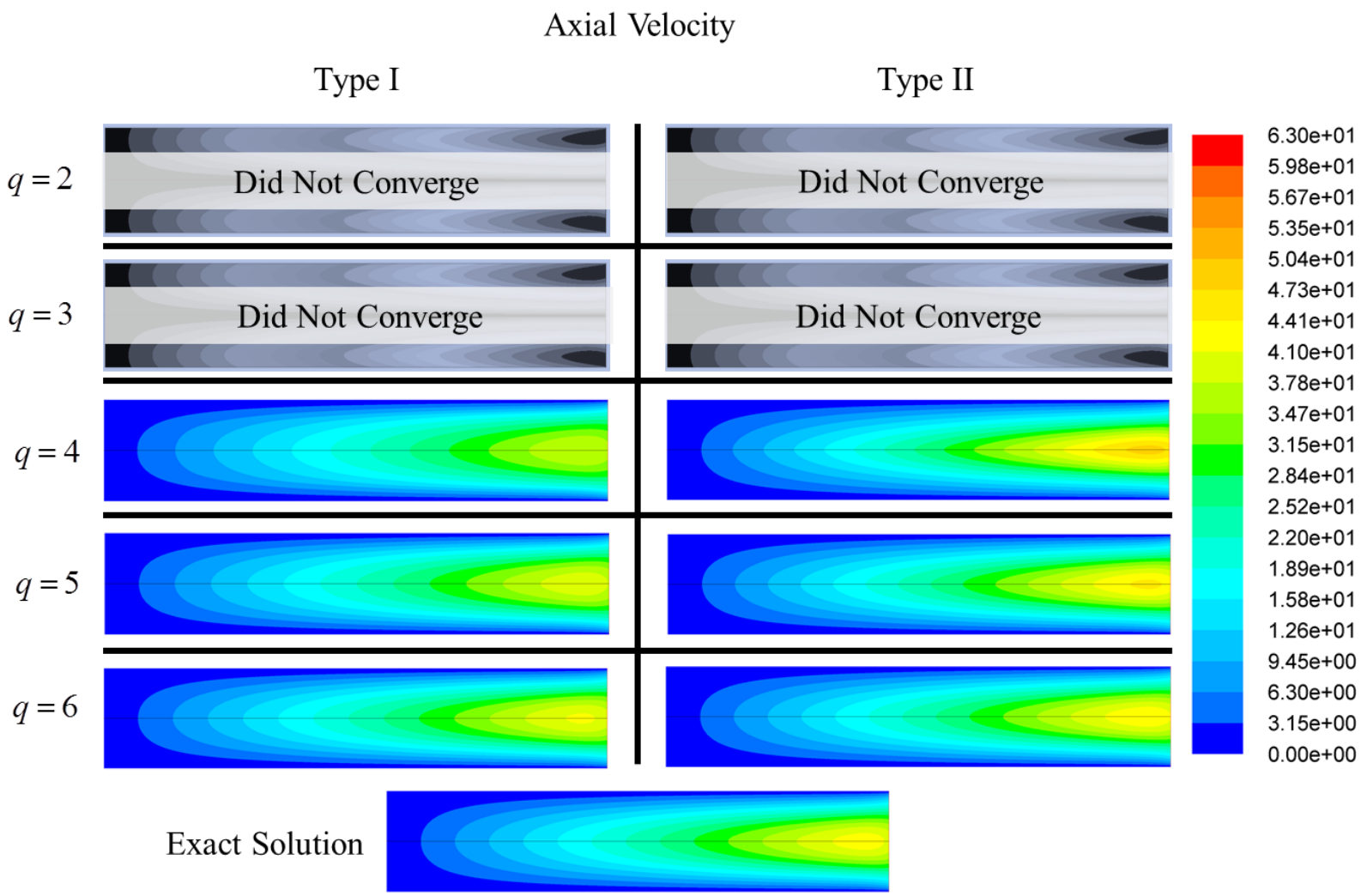


**Figure B.8 Comparison of Contours for Energy-Optimized Type I, Type II and Exact Solutions - Axial Velocity**

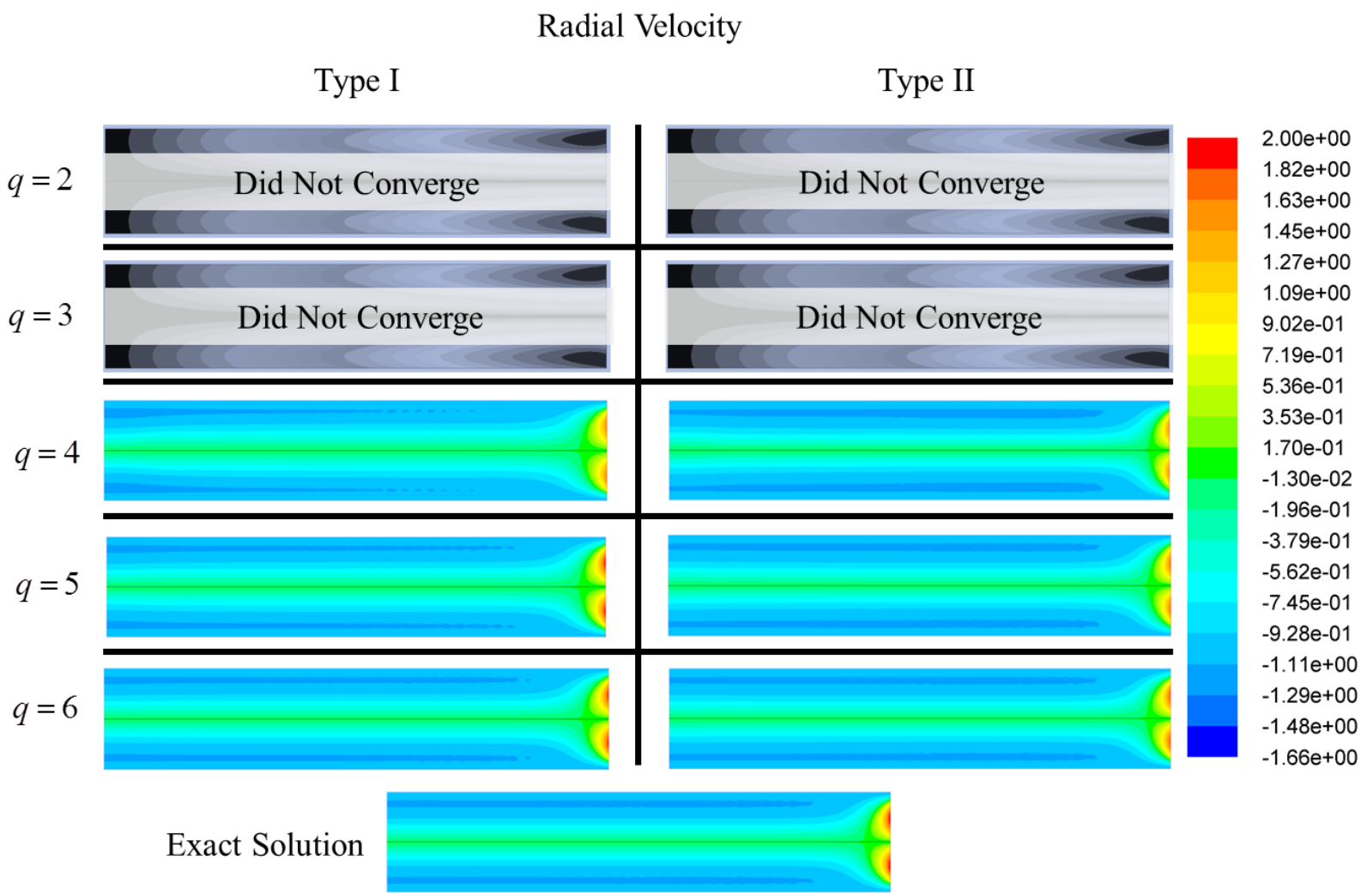


**Figure B.9 Comparison of Contours for Energy-Optimized Type I, Type II and Exact Solutions - Axial Velocity**

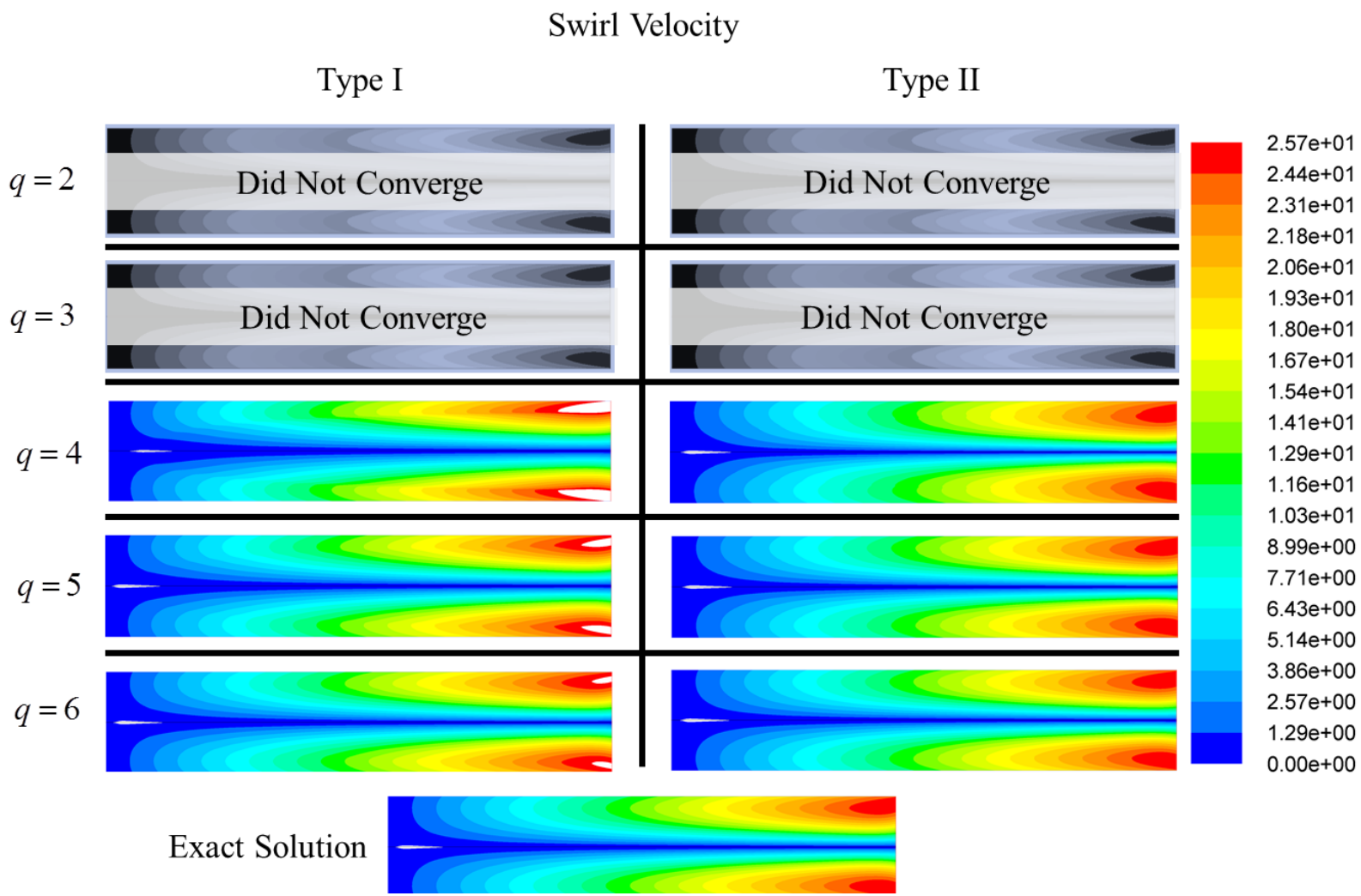


**Figure B.10 Comparison of Contours for Energy-Optimized Type I, Type II and Exact Solutions - Swirl Velocity**

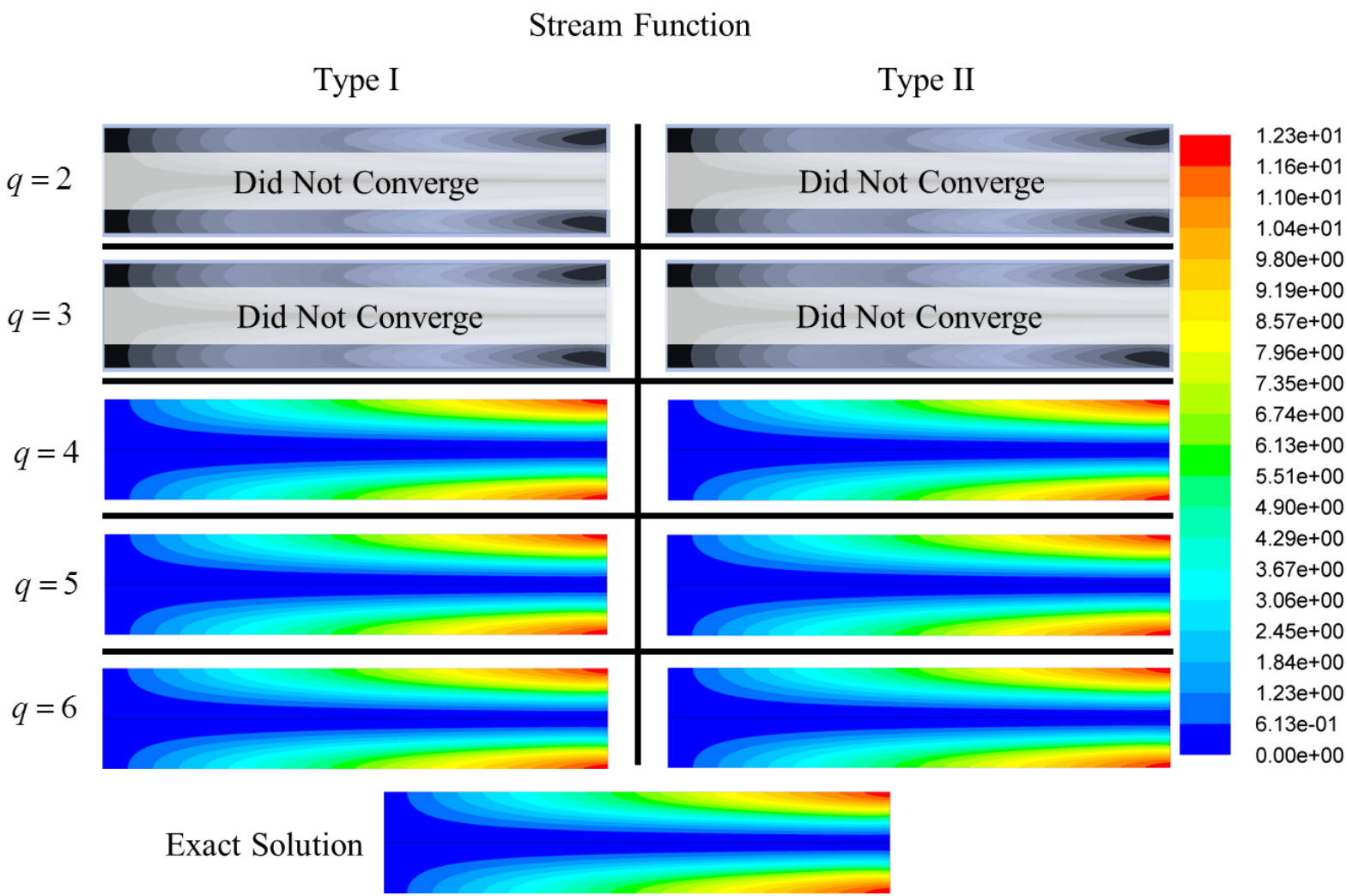


**Figure B.11 Comparison of Contours for Energy-Optimized Type I, Type II and Exact Solutions – Stream Function**

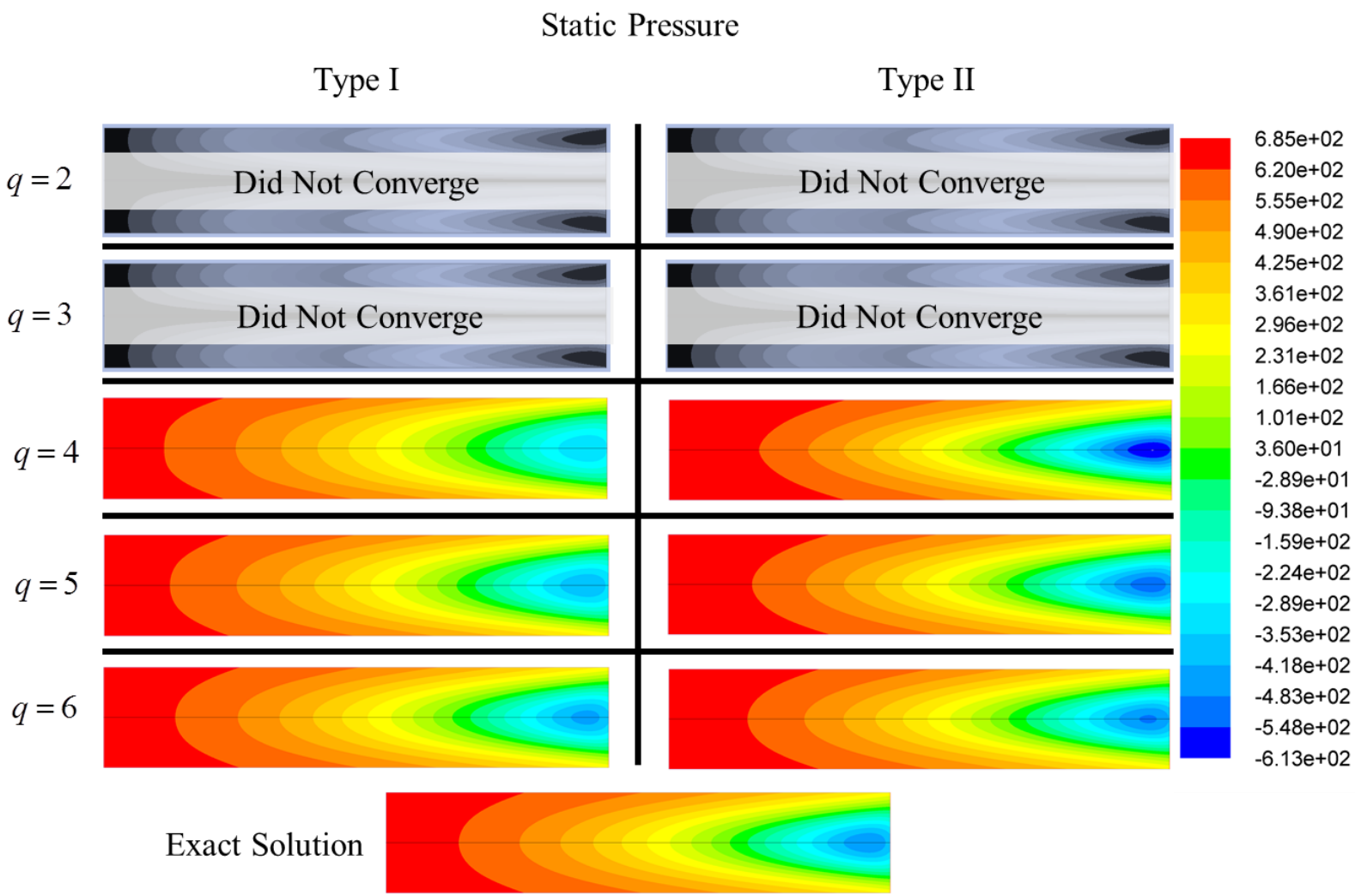


**Figure B.12 Comparison of Contours for Energy-Optimized Type I, Type II and Exact Solutions – Static Pressure**

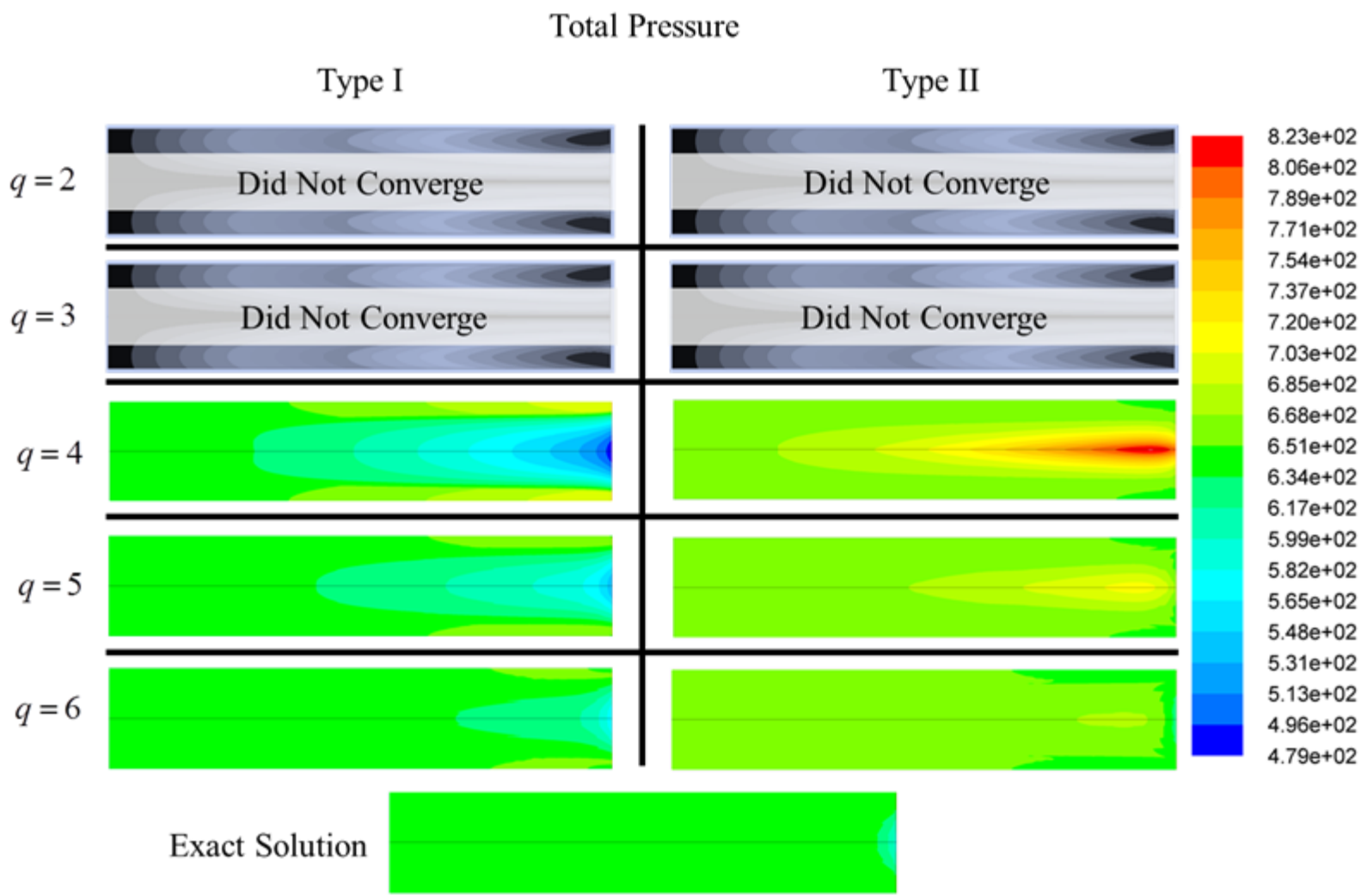


**Figure B.13 Comparison of Contours for Energy-Optimized Type I, Type II and Exact Solutions – Total Pressure**

# Vita

Andrew Steven Fist received a Bachelor of Mechanical Engineering degree from the University of Dayton in December 2009. Andrew joined the University of Tennessee Space Institute in 2010 where he studied Mechanical Engineering under the advisement of Dr. Majdalani, and will graduate with a Master of Science in Mechanical Engineering degree in 2016.